J. Fluid Mech. (2012), *vol.* 693, *pp.* 508–540.
doi:10.1017/jfm.2011.547

Crumpled water bells

H. Lhuissier and E. Villermaux†‡

Aix-Marseille Université, IRPHE, 13384 Marseille CEDEX 13, France

(Received 27 July 2011; revised 4 November 2011; accepted 9 December 2011;
first published online 24 January 2012)

Stationary axi-symmetrical pressurized bells formed by the impact of a liquid jet on a solid disc (so-called Savart water bells) can exhibit uncommon sharp and pointed shapes. They are characterized by two successive inflections of the two-dimensional bell generator profile, corresponding to partially concave bells. We show that this shape is incompatible with the usual assumption that the detail of the flow across the liquid sheet constitutive of the bell is unimportant. We consider the equilibrium of a curved liquid sheet of *finite* thickness sustaining a pressure difference between both sides, and show that several curvatures of the interface may be a solution under given flow conditions. The inflection of the bell profile is then explained in terms of a spontaneous transition from a 'negative' to a 'positive' curvature which conserves mass flow, linear and angular momenta. That inflection is also a transition from a super to a subcritical flow (with respect to capillary waves), having the status of a capillary hydraulic jump on a *freely suspended* sheet, a novel object in fluid mechanics. The azimuthal wrinkles forming at the jump result from the inertial destabilization of the sheet due to the centripetal acceleration fluid particles experience as they flow along the highly curved bell profile in the vicinity of the fold. This finding also explains the singular shape at the edge of freely flapping sheets.

Key words: general fluid mechanics, interfacial flows (free surface), thin films

1. Introduction

Liquid bells were first evidenced by Félix Savart in his *Mémoire sur le Choc d'une Veine liquide lancée contre un plan circulaire* (Savart 1833*a*,*b*). His postulate was that studying the macroscopic shapes of deviated liquid streams would provide information about the nature of the cohesion forces between the 'molécules' in the liquid (the word 'molécule' has to be understood in the sense of Laplace 1805 as a synonym of 'fluid particle'; the atomistic molecular interpretation of cohesion will come soon after, see e.g. Rowlinson 2002). Figure 1 represents some of the stable liquid bells Savart described by letting a liquid jet impact normally on a flat solid disc. By varying the jet and impacting disc diameters, the liquid velocity and the pressure inside the bell, Savart observed various shapes, among which we have the one labelled '*Fig.* 16', which exhibits sharp curvatures particularly uncommon for a liquid. It is precisely this singular shape that we intend to explain here. We refer to those bells as 'crumpled bells' and refer to the region of sharp curvature localized around the maximal radial extension of the bell as a 'fold'. The main feature of these bells is to be partially

† Email address for correspondence: villermaux@irphe.univ-mrs.fr
‡ Present address: Also at Institut Universitaire de France.

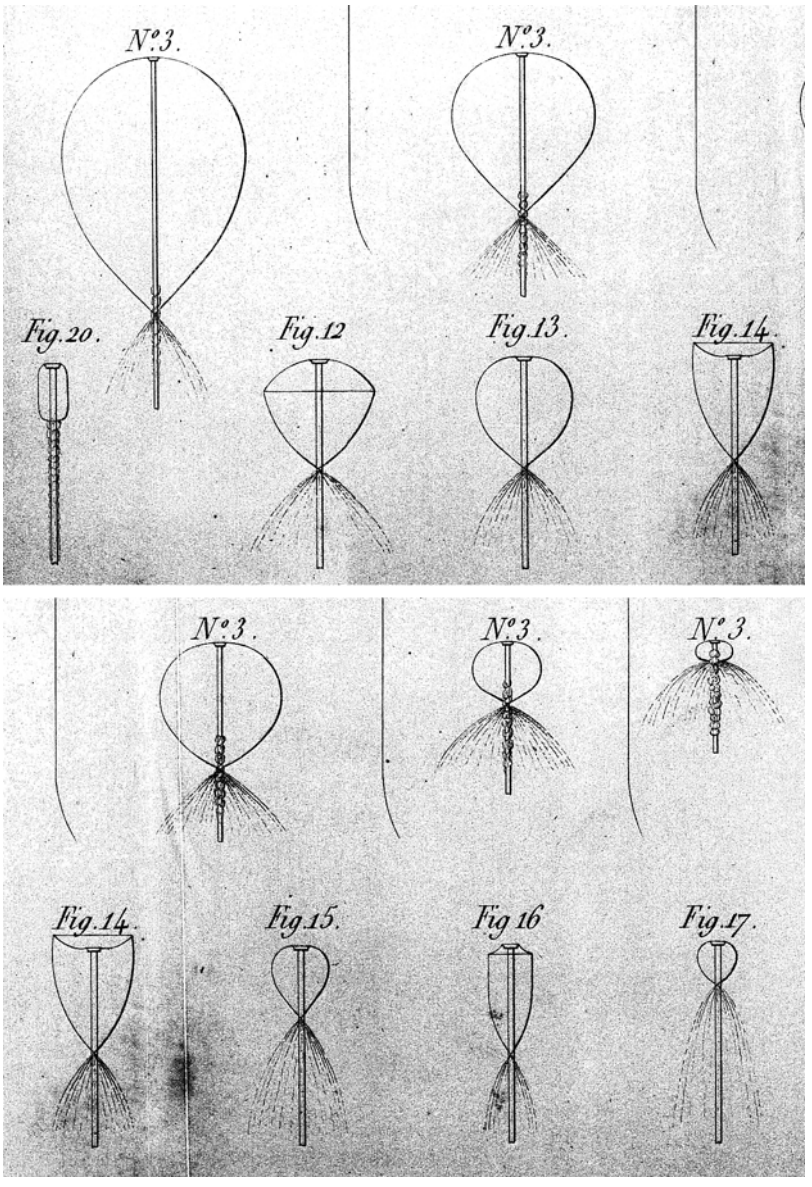

FIGURE 1. Experimental bell profiles reported by Savart (1833*a*) (the jet, impinging from above is not drawn). Note the partially concave, stationary bell labelled '*Fig. 16*': a horizontal line representing an angle or sharp curvature separates the upstream (top) concave portion from the downstream (bottom) convex portion of the bell.

concave: their radial profile has two inflection points, the second one being located at the fold; figure 2 shows a picture of a crumpled bell where this is clearly visible.

Savart's works were the first of a long series. Assuming a symmetry of revolution, Boussinesq (1869*a*,*b*) put the shape of liquid bells in equation form. He considered the situation of equal inner and outer pressure and found, in the absence of gravity, that a catenoid is a solution. Without detailing it, Boussinesq implicitly adopted the *a priori* reasonable hypothesis that the liquid streamlines curvature is approximately the same

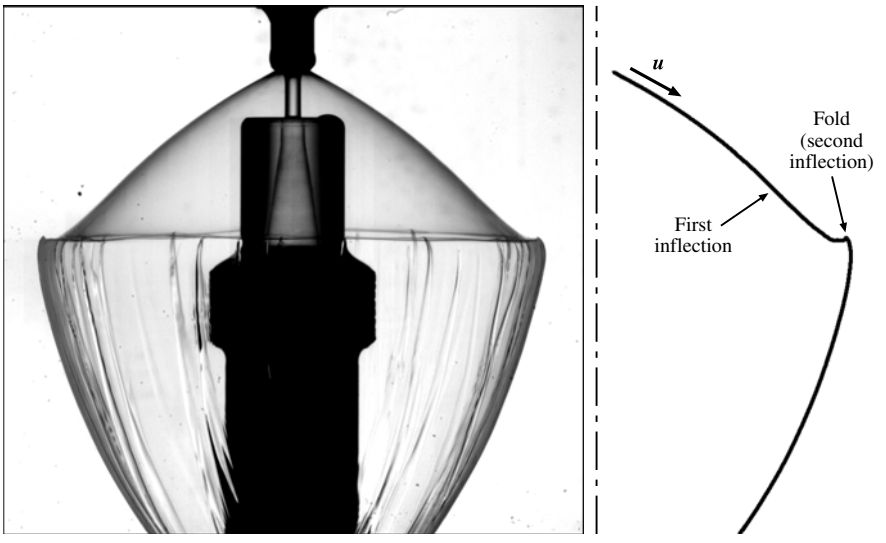

FIGURE 2. A crumpled liquid bell formed with tap water (with surface tension $\sigma = 73 \times 10^{-3}$ N m^{-1}, density $\rho = 10^3$ kg m^{-3} and dynamic viscosity $\eta = 10^{-3}$ kg m^{-1} s^{-1}). The upward jet in the centre (with diameter $d_0 = 3$ mm and Weber number $We_0 = 230$) is deflected as it impacts the top solid cylinder (with diameter $d_d = 6$ mm) and forms a stationary, globally axi-symmetrical, downward flowing liquid sheet collapsing on the axis (below the picture bottom), a closed liquid bell. From top to bottom (streamwise) the bell is convex then concave at the first inflection point just before the fold and then convex again at the second inflection point, the fold. Image width is 106.7 mm.

all across the liquid sheet in a given transverse section; that is to say that the sheet thickness h is everywhere negligible with respect to its characteristic local radius of curvature κ_θ^{-1},

$$\kappa_\theta h \ll 1. \tag{1.1}$$

Liquid bells have enjoyed a continuing interest in the 20th century because they were expected to allow for precise measurements of the interface contamination rates through the bell shape dependence on surface tension (Bond 1935; Puls 1936; Bond & Puls 1937). Later, Hopwood (1952) and Lance & Perry (1953) observed angular bells identical to our crumpled bells that they interpreted as non-physical solutions of the bell shape equations (again in the limit $\kappa_\theta h \ll 1$) whose generator profiles present a loop. Taylor (1959*a*) discussed the influence of the cavity air flow on the bell shape, and Parlanges (1967) applied his calculations to clarify the discrepancy between measured and expected bell shapes.

More recently, Buckingham & Bush (2001) observed a polygonal water bell using a viscous liquid (up to 100 times more viscous than water). The corresponding mechanism may differ from the one we present here for crumpled water bells, as it may also be a manifestation of the viscous buckling of the sheet, and/or of an axi-symmetry breaking in the injection conditions. Clanet (2001) studied the stability of water bells with respect to cavity pressure fluctuations, and determined an expression for the pressure difference threshold above which the generator profile presents a non-physical loop before rejoining the bell axis. We show in § 2 that this expression is not valid for all injection conditions, and derive the correct criterion valid in the whole parameter space. Using a very large impact disc, Brunet, Clanet & Limat (2004)

obtained subcritical stable water bells, i.e. bells whose flow velocity u is smaller than the propagation velocity of sinuous capillary waves $V = \sqrt{2\sigma/\rho h}$, coinciding with the Taylor–Culick receding velocity of a free sheet edge. We show in § 4.2 that crumpled bells necessarily develop a portion of subcritical flow, explaining also their fragility.

Following Boussinesq, every mathematical model of liquid bells has been based on the assumption in (1.1) until Clanet (2007) attempted to consider the detail of the flow across the sheet, to finally conclude that it can be disregarded for the usual bell shapes. In contrast, we focus on unusual shapes for bells, and develop the point of view that the sharply curved crumpled bells cannot be understood without accounting for the details of the flow across the sheet, and that the double inflection of their profile cannot be explained within the usual paradigm (1.1).

Anticipating the development of the present work, we need to introduce works on capillary hydraulic jumps. Not surprisingly, we start again with Savart (1833*b*) who reported the phenomenon for the first time. In the same series of experiments we already referred to, Savart studied the influence of the impact disc diameter. Between the centre and the border of the disc, the behaviour of the liquid sheet in contact with the solid differs from that in the bell, where it is suspended in air. For large impact disc diameters, this leads to the onset of a sudden thickening of the sheet at a definite radius, known as a hydraulic jump. It corresponds to a transition from a supercritical to a subcritical flow with respect to capillary-gravity waves propagating over a layer of finite depth at a velocity of order $\sqrt{gh}$, where g is gravity. We show in § 4.2 that, surprisingly, the contact with a solid wall is not a mandatory condition for the onset of a hydraulic jump: the conjunction of the curvature of the liquid sheet with the pressure difference between its two interfaces requires the sudden transition to a subcritical flow regime.

The circular hydraulic jump occurring on the radially expanding liquid layer formed from the impact of a jet on a flat surface has been the subject of numerous studies, with the determination of the jump radius as a main concern. Watson (1964) and Bohr, Dimon & Putkaradze (1993) considered the case of negligible surface tension (relevant for layer thicknesses larger than the capillary length $\sqrt{\sigma/\rho g}$) and Bush & Aristoff (2003) considered the corrections due to surface tension for thin layers. The departure from axi-symmetry (Ellegaard *et al.* 1998) and the stability (Bush, Aristoff & Hosoi 2006) of capillary hydraulic jumps have also been studied, but to our knowledge the possibility of an hydraulic jump occurring on a *suspended* liquid sheet, that is to say without a direct contact with a solid wall, has never been reported.

In § 2 we recall the bell shapes that are expected in the usual limit $\kappa_\theta h \ll 1$ and the precise injection conditions to form closed bells. In § 3, we show that crumpled bell shapes are incompatible with the assumption $\kappa_\theta h \to 0$ and explain how considering the flow across the sheet allows for new solutions. In § 4 we show that a sudden transition between two such solutions, separating respectively a supercritical from a subcritical flow region, explains the second inflection of the bell generator profile and at the same time the existence of crumpled liquid bells. Lastly, § 5 is dedicated to the wrinkles developing at the hydraulic jump; a classical inertial mechanism explaining their formation is discussed. We conclude by extending the above ideas to the context of liquid sheets (i.e. 'open bells') at large Weber number in the flag-like flapping regime, for which sharply curved folds and wrinkles are the rule at the sheet edge.

2. Usual equations and shapes

2.1. *Basic equations*

In the most general case, a closed liquid bell is shaped by an equilibrium between liquid inertia, surface tension, gravity and pressure difference between the inside and

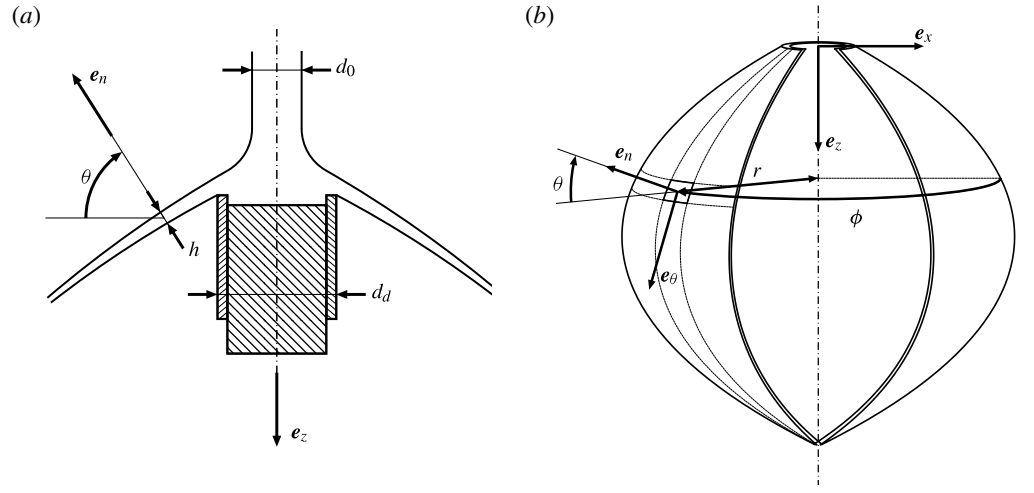

FIGURE 3. (*a*) Section of the jet and impact disc, showing the thin corona whose vertical offset is adjusted to set the desired sheet deflection angle θ_0. (*b*) Bell coordinates system.

the outside. We consider here an axi-symmetrical bell formed by the normal impact of a cylindrical jet of diameter d_0 on a solid disc of diameter d_d, as sketched in figure 3. The velocity u_0 of the jet is uniform and constant. We consider bells of radial extension $L \gg d_0$ and, except for the possible folds we consider later, the sheet thickness h is everywhere negligible in comparison with the radius of curvature of order L. We indeed adopt here the usual hypothesis $\kappa_\theta h \ll 1$ as a starting point in order to show its direct implications. In that limit the velocity $\boldsymbol{u}$ is uniform across the liquid sheet so that the flow is fully described by the two scalars

$$\begin{cases} h = h(s) \\ \boldsymbol{u} = u(s)\boldsymbol{e}_\theta \end{cases} \tag{2.1}$$

depending on a single coordinate s that parametrizes the two-dimensional bell generator profile $\{r(s), z(s)\}$, where r is the distance to the symmetry axis and z the vertical downward distance from the impact disc. This coordinate system allows for the description of possible folding and looping of the bell profile.

As long as the boundary layer thickness of order $\sqrt{\nu d_d/u_0}$ developing at the disc surface is small compared with the inviscid estimate of the liquid layer thickness $h \sim d_0^2/d_d$, viscous friction can be disregarded. This condition similarly writes $Re\,(d_0/d_d)^3 \gg 1$, where $Re = u_0 d_0/\nu$ is the jet Reynolds number, and is always verified in the following. Dissipation is *a fortiori* negligible in the suspended part of the bell where the shear stress with the air is essentially negligible (except around sharp sheet curvatures, as we discuss later). For gravity $\boldsymbol{g} = g\boldsymbol{e}_z$ pointing in the same direction as the jet velocity, energy and mass conservation give

$$\begin{cases} h = \dfrac{d_0^2}{8r}\dfrac{u_0}{u} \\ u = u_0\sqrt{1 + \dfrac{2g}{u_0^2}z}. \end{cases} \tag{2.2}$$

Let us make the inventory of the strains in the normal direction $\boldsymbol{e}_n$ an elementary portion of the bell is subjected to (see figure 3):

(*a*) for a given curvature κ_θ in the plan $(\boldsymbol{e}_n, \boldsymbol{e}_\theta)$, the flowing liquid sustains the centripetal acceleration $\kappa_\theta u^2$; multiplied by the sheet surface mass ρh, this yields $\rho h \kappa_\theta u^2$ for the liquid inertia;

(*b*) surface tension forces depend on the local principal curvatures κ_θ and κ_ϕ to give the capillary pressure $-2\sigma(\kappa_\theta + \kappa_\phi)$, where the factor 2 accounts for the inner and outer interfaces;

(*c*) pressure difference between the inside and outside of the bell gives the contribution $\Delta p = p_i - p_e$;

(*d*) finally, the weight $\rho \boldsymbol{g} h$ when projected upon $\boldsymbol{e}_n$ writes $-\rho g h \sin\theta$.

The relevant length scale is the bell maximal radial extension $L = We_0 d_0/16$ where the Weber number

$$We_0 = \frac{\rho u_0^2 d_0}{\sigma} \tag{2.3}$$

compares liquid inertia with surface tension forces. Here L represents the radius beyond which surface tension forces overcome the flow momentum rate; it is indeed the equilibrium radius of a planar liquid sheet formed when the ejection angle is $\theta_0 = \pi/2$ (Taylor 1959*b*). Non-dimensionalizing lengths and times by L and L/u_0, respectively, and expressing the curvatures $\kappa_\theta = -\partial_s\theta$ and $\kappa_\phi = \cos\theta/r$ in terms of the angle θ between the profile tangent and the vertical (see figure 3), one gets the following system prescribing the bell shape (by momentum conservation perpendicular to the direction of the flow)

$$\begin{cases} \dfrac{\partial\theta}{\partial s}\left(\sqrt{1+\dfrac{Bo}{8}z} - r\right) = -\cos\theta + Pr - \dfrac{Bo}{16}\dfrac{\sin\theta}{\sqrt{1+\dfrac{Bo}{8}z}} \\ \dfrac{\partial r}{\partial s} = \sin\theta \quad \text{and} \quad \dfrac{\partial z}{\partial s} = \cos\theta \end{cases} \tag{2.4}$$

where $P = (p_i - p_e)We_0 d_0/32\sigma$ is the dimensionless pressure difference and the Bond number $Bo = \rho g d_0^2/\sigma$ compares gravity with surface tension.

Remaining in the domain where viscosity has no influence, the bell shape is determined by five parameters: We_0, Bo, P, d_d/d_0 and θ_0 the sheet orientation at the impact disc edge. A sixth parameter, namely the ratio of the air to liquid densities ρ_a/ρ has also to be considered if ambient atmosphere is expected to interact significantly with the bell, a configuration we do not consider here until the conclusion (see figures 18 and 20). With such a broad parameter space, the large variety of shapes Savart observed seems quite natural.

2.2. *Some simple shapes*

For large jet velocity, gravity can be forgotten and the liquid velocity is conserved all along the bell profile. Imposing $Bo = 0$, (2.4) then takes the simplified form

$$\begin{cases} \dfrac{\partial\theta}{\partial s}(1-r) = -\cos\theta + Pr \\ \dfrac{\partial r}{\partial s} = \sin\theta. \end{cases} \tag{2.5}$$

An invariant quantity can be derived from this system since everywhere on the bell

$$(1-r)\cos\theta + \frac{P}{2}r^2 = cte \equiv (1-r_0)\cos\theta_0 + \frac{P}{2}r_0^2. \tag{2.6}$$

In the particular case of a bell cavity maintained at atmospheric pressure, that is to say $P=0$, (2.6) can be integrated again to obtain an explicit expression for the altitude z as a function of the radius r

$$z(r) = (1-r_m)\ln\left(\frac{\dfrac{1-r_m}{1-r}}{1+\sqrt{1-\left(\dfrac{1-r_m}{1-r}\right)^2}}\right) \tag{2.7}$$

where $r_m \leqslant 1$, the maximal radius actually reached by the bell, can be expressed directly in terms of the initial conditions at the impact disc edge r_0 and θ_0 from (2.6). This is the solution Boussinesq (1869*a*,*b*) obtained. It identifies with the celebrated catenoid since (2.7) can be equivalently written as

$$\frac{1-r}{1-r_m} = \cosh\left(\frac{z-z_m}{1-r_m}\right) \tag{2.8}$$

with z_m being the downstream altitude at which the maximal radius r_m is reached. By symmetry $2z_m$ is also the altitude at the sheet collapses on its axis.

2.3. *More complex shapes*

As already mentioned, a pressure difference can be imposed between the atmosphere and the closed bell cavity, allowing for the various shapes figure 1 illustrates. The generator profiles $\{r(s), z(s)\}$ may then present inflection points, and one may observe bells that are not globally convex any more (note that it is also theoretically possible to obtain partially concave bells when $P=0$, but only when gravity is important and those bells, unstable with respect to any pressure or inclosed volume fluctuation, are generally not stationary; Clanet 2001). This behaviour is included in the usual model adopted in (2.5) where the pressure term can actually make the right-hand side positive, changing so the sign of the curvature $\partial_s\theta$. The condition for inflection can thus be written

$$P = \frac{\cos\theta}{r} \tag{2.9}$$

which simply expresses that the curvature κ_θ vanishes when the excess pressure Δp balances the capillary pressure $2\sigma\kappa_\phi$.

Starting from a locally convex bell at the disc edge (i.e. $\partial_s\theta < 0$), a globally convex bell shape requires that inflection does not occur anywhere (this is also a sufficient condition). The condition $P \leqslant \cos\theta$ must therefore be verified for every point of the profile and not only for $\theta = 0$ in $r = r_m$ as supposed by Clanet (2001, 2007), leading to a too restrictive inflection criterion equivalent to the global criteria we derive here only for a particular range of injection conditions.

That inflection occurs at a given point $\{r, \theta\}$ of the bell profile requires that $r = \cos\theta/P$ according to (2.9), and also that r and θ be a solution of (2.6). The *local* critical pressure $P \equiv f(\cos\theta)$ which is a solution of the latter system ((2.9) and (2.6)) can be straightforwardly expressed in terms of $\cos\theta$. The *global* condition for an inflection of the profile is then to be found at the most penalizing point where

the pressure locally required to trigger the inflection is the smallest, that is to say where f is minimal. For given initial conditions r_0 and θ_0, this critical point, where $\partial_{\cos\theta} f = 0$, verifies

$$\cos\theta_c = \frac{2\cos\theta_0}{1+r_0}. \tag{2.10}$$

This expression is only valid in the range $\theta_0 \geqslant \arccos[(1+r_0)/2]$. In that case, according to (2.6), the limit pressure P_c above which inflection appears for the first time somewhere on the profile is

$$\begin{cases} P_c = f(\cos\theta_c) = \dfrac{2\cos\theta_0}{1+r_0} \\ \text{for } \theta_0 \geqslant \arccos\left(\dfrac{1+r_0}{2}\right). \end{cases} \tag{2.11}$$

By comparison with (2.9) it appears that, for the above range of injection conditions, the onset of inflection actually occurs in $r \to r_m = 1$ but *not* in $\theta = 0$. For the critical pressure P_c the profile shape around the maximal radius indeed consists in a corner with half angle $\pi/2 - \theta_c$ (see figure 4) and inflection thus occurs immediately upstream from that corner, where $r/\cos\theta$ is minimal and promotes the inflection.

In the opposite case of a small deflexion angle by the impact disc, that is to say when $\theta_0 \leqslant \arccos[(1+r_0)/2]$, no corner is formed in the profile and condition (2.9) is the most restrictive at the maximal extension in $\theta = 0$. The global criterion then becomes equivalent to the one Clanet determined by considering the condition at this point only, and can be written as

$$\begin{cases} P_c = \dfrac{1-(1-r_0)\cos\theta_0}{r_0^2}\left(1-\sqrt{1-\dfrac{r_0^2}{[(1-r_0)\cos\theta_0-1]^2}}\right) \\ \text{for } \theta_0 \leqslant \arccos\left(\dfrac{1+r_0}{2}\right). \end{cases} \tag{2.12}$$

Expressions (2.11) and (2.12) together correctly predict the onset of an inflection of the generator profiles we obtained by numerical integration of (2.5), that is to say when $Bo = 0$, for the whole range of initial conditions. Figure 4 shows six of those profiles, together with their equivalents obtained under non-vanishing gravity, for a Bond number comparable with that in our experiments and for two distinct deflection angles θ_0. It illustrates that in the case of large deflection angles, i.e. when $\theta_0 \leqslant \arccos[(1+r_0)/2]$, the transition to a reversing of the profile proceeds, as already mentioned, by continuously decreasing the local radius of curvature at the bell maximal radius but otherwise conserving a global bell shape of finite size. By contrast for small deflection angles, i.e. when $\theta_0 < \arccos[(1+r_0)/2]$, the transition to the formation of a loop proceeds by elongating the bell profile up to a theoretically infinite value. This transition is also observed experimentally, but it never leads to a crumpled shape since the bell, thus looking like a long hollow jet, destabilizes by a Rayleigh–Plateau-like mechanism. For that reason only crumpled bells with $\theta_0 > \arccos[(1+r_0)/2]$ corresponding to (2.11) can be obtained, and we therefore only consider this case in the following.

The main point here is that according to (2.5) an inflection of the profile (determined by the condition $P > P_c$) irremediably implies the formation of a loop. Indeed, the curvature variation with r can be reformulated into the more explicit

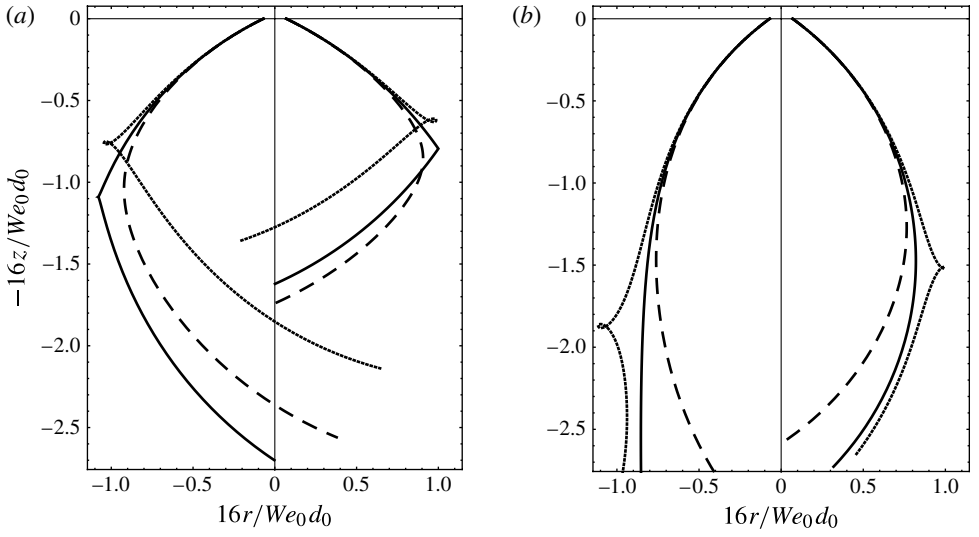

FIGURE 4. (*a*) Bell generator profiles for conditions close to that triggering the reversing obtained by numerical integration of system (2.4). The parameters are the same as those of the experimental bell shown in figure 5, that is to say $We_0 = 230$, $r_0 = 0.07$ and $\theta_0 = 64° > \arccos[(1 + r_0)/2] = 57°$. For profiles on the left-hand side ($r < 0$) $Bo = 13.8$ (the experimental value) and the inside pressure is successively the critical value $P_{c,g} = 0.90$ (plain line), $P_{c,g} + 0.05$ (dotted line) and $P_{c,g} - 0.05$ (dashed line). For profiles on the right-hand side ($r > 0$) the Bond number is zero and inside pressure is successively $P_c = 0.82$, determined using (2.11), and $P_c \pm 0.05$. (*b*) For comparison, the transition to the reversing for small deflection angle $\theta_0 < \arccos[(1 + r_0)/2]$ proceeds by a theoretically infinite elongation of the bell (which is experimentally observed until the bell destabilizes by a long-wave Rayleigh–Plateau-like mechanism). The conditions are the same as in the graphics on the left-hand side except for $\theta_0 = 54°$ and for the pressures which are $P_{c,g} = 1.15$ and $P_{c,g} \pm 0.025$ for the left-hand part and $P_c = 1.10$ and $P_c \pm 0.025$ for the right-hand part.

expression

$$\frac{\partial}{\partial r}\frac{\partial \theta}{\partial s} = \frac{P + 2\dfrac{\partial \theta}{\partial s}}{1 - r} \tag{2.13}$$

where one sees that starting with $\partial_s\theta < 0$ at the impact disc edge, the sign of $\partial_s\theta$ may change a first time as r increases (a condition that requires $P > 0$) but not a second time before the maximal extension $r = r_m$ is reached. Indeed according to (2.13) after a first inflection $\partial_{r,s}\theta$ is positive since both $\partial_s\theta$ and P are positive. This means an unphysical loop (since it implies that the liquid sheet would cross itself without interacting) is realized before the profile reaches back the axis and closes the bell. As figure 4 shows, the behaviour is the same whether gravity is present or not.

Therefore, according to (2.4), inflection and unphysical looping of the bell profile cannot be observed independently one from the other.

3. The role of thickness

In light of the above remark, we naturally conclude that crumpled bells that do show an inflection of their profile, but obviously do not intersect themselves, cannot be understood on the basis of (2.5), that is to say on the basis of the above-mentioned

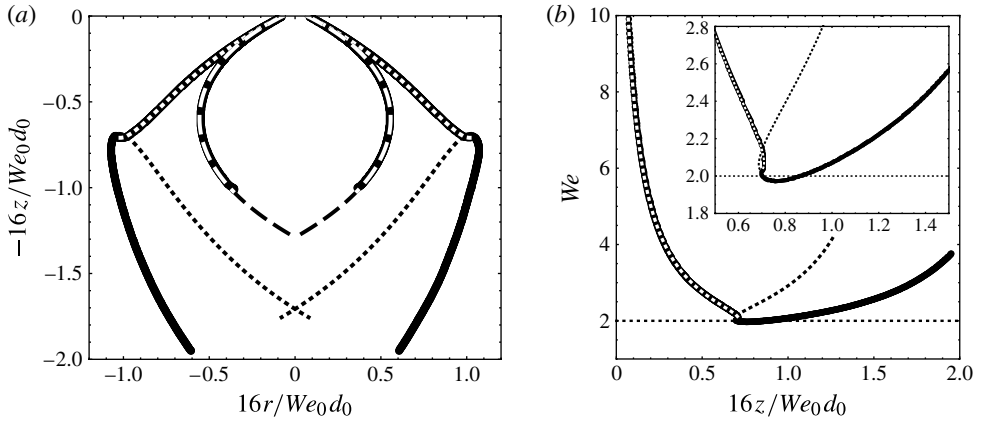

FIGURE 5. (*a*) Experimental profile (dots) and profile resulting from the numerical integration of (2.4) (dotted line) of a crumpled bell. The jet diameter and Weber number are $d_0 = 3$ mm and $We_0 = 230$ respectively. Experimental (dots) and numerical (dashed line) profiles for the same bell once a zero pressure difference $\Delta p = 0$ has been imposed by connecting inside with outside. The only non-independently measured parameter is the pressure difference Δp of the first profile that we determine by fitting the experimental profile with the numerical one upstream from the fold. (*b*) Local Weber number for experimental (dots) and numerical (dotted line) profiles for the same bell as in the graphics on the left-hand side. The Weber number $We = \rho h u^2/\sigma$ is computed from expressions for u and h defined in (2.2), i.e. $We = \sqrt{1 + 2gz/u_0^2}\, We_0 d_0/8r$.

usual assumption $\kappa_\theta h \to 0$. To the best of the authors' knowledge they have not been explained on any basis although they have been visible on the almost 200-year-old Savart plates (see figure 1) where the drawing labelled '*Fig. 16*' clearly represents a bell whose first concave part is separated from a second convex part by a 'sharp transition' that Savart sketched as an horizontal line. This shape has been observed later by Hopwood (1952), Lance & Perry (1953) and Clanet (2001, 2007) notably. One of our own observations is shown in figure 2.

In order to explain the second inflection of the profile (mandatory to account for the absence of the sheet looping and self-destruction) that is observed on crumpled bells, we consider the phenomena associated with a finite thickness h comparable with the local radius of curvature $R \equiv \kappa_\theta^{-1}$ of the sheet. This point of view is motivated by the observation of very small local radii of curvature R close to the maximal radius of the bell, precisely where the experimental shape is seen to depart strongly from the theoretical shape based on the assumptions $\kappa_\theta h \ll 1$. This more detailed description leads to a new equilibrium equation for the liquid sheet that differs from that underlying equation (2.4). If we suppose that both interfaces are locally parallel and call R_m the median line radius of curvature (see figure 6), this equilibrium along their joint normal $\boldsymbol{e}_n$ writes

$$p_i - \frac{\sigma}{R_m - \dfrac{h}{2}} + \int_{R_m-(h/2)}^{R_m+(h/2)} \frac{\rho u^2}{R}\,\mathrm{d}R - \frac{\sigma}{R_m + \dfrac{h}{2}} = p_e \tag{3.1}$$

where the influence of the azimuthal curvature $\kappa_\phi \ll \kappa_\theta$ and that of gravity have been neglected. This approximation is justified by the relative magnitude of radii of curvature $\kappa_\theta^{-1} \sim 1$ mm and $\kappa_\phi^{-1} \sim 100$ mm at the maximal radius of the bell where we

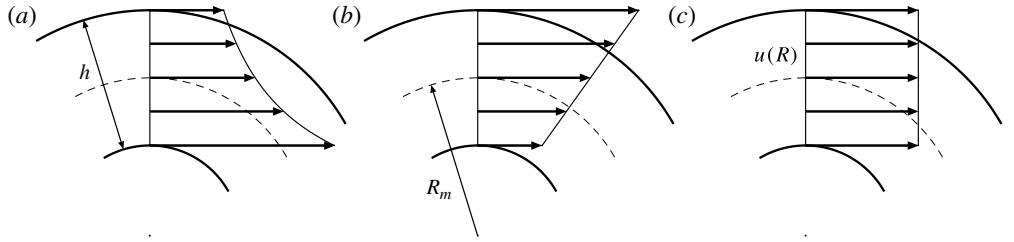

FIGURE 6. Various characteristic velocity profiles $\boldsymbol{u} = u(R)\boldsymbol{e}_\theta$ in the transverse cross-section of the liquid sheet. (*a*) Zero vorticity profile expected for a vanishing viscosity, $u(R) = u_m\,(R/R_m)^{-1}$. (*b*) Zero shear profile expected for an infinite viscosity, $u(R) = u_m R/R_m$. (*c*) 'Intermediate' profile, $u(R) = u_m$.

invoke finite thickness effects to explain the second inflection one can see in figure 2. In the same way, the gravity term $\rho g h \sim 10^{-1}$ Pa is negligible with respect to the pressure difference $\Delta p \sim 1$ Pa.

In the limit $h \ll R_m$ (equivalent to $\kappa_\theta h \ll 1$), valid all over the profile except at the fold, integration in (3.1) is achieved at an essentially constant radius R, since inner and outer curvatures coincide, and one naturally recovers the terms in (2.4) whatever the velocity profile $\boldsymbol{u} = u(R)\boldsymbol{e}_\theta$ across the sheet section may be, as long as it can be integrated. On the other hand when the ratio h/R_m is not negligible any more, as it is actually the case at the fold, the transverse equilibrium (3.1) between inertial and capillary forces directly depends on the law $u(R)$, which thus needs to be discussed.

In the limit of vanishing viscosity and by virtue of Kelvin's theorem, the vorticity of a fluid element is a conserved quantity from the point where it leaves the impact disc to the point where it collapses on the symmetry axis. If we consider, in accordance with the condition $Re\,(d_0/d_d)^3 \gg 1$ expressing that shear stress at the impact disc is negligible, that the velocity profile across the thickness is uniform at the disc edge, the initial condition is that of a zero vorticity for a initial curvature R_m^{-1} we can neglect. If vorticity $\partial_R(Ru)/R$ were actually a conserved quantity, one would expect that in every cross-section of the liquid sheet the velocity profile would depend only on the streamlines local radius of curvature according to $u(R) = u_M\,(R/R_M)^{-1}$ (see figure 6), where the velocity u_M is that of the reference streamline coinciding with the sheet median line (which may vary with the profile abscissa s).

Conversely, for a large liquid viscosity, momentum diffuses across the sheet and cancels the shear more rapidly than the streamlines curvature evolution builds it as the liquid follows the bell profile. The velocity profile resulting from a viscosity dominated flow is thus a shear-less profile verifying $(\partial_R u - u/R)/2 = 0$, that is to say a solid body velocity field $u(R) = u_M R/R_M$.

For the bells we are considering, the viscous relaxation time h^2/ν and the characteristic curvature evolution time $(u\partial_s \ln \kappa_\theta)^{-1} \sim (\kappa_\theta u)^{-1}$ are both of the same order of magnitude at the fold location, that is 10^{-3} s. We thus consider that a good approximation of the actual velocity profile is the 'intermediate' one between the two opposite limits above, which turns out also to be the simplest

$$u(R) = u_M = u \tag{3.2}$$

defining a uniform velocity profile across the sheet. In doing so, we use (consciously) the same velocity profile Newton (1687) had erroneously derived for the azimuthal flow around a cylinder rotating in a viscous fluid (see Newton 1687, Book II, Prop. 51, and Darrigol 2005, p. 105). Note finally that more generally and for the reasons

we discuss below, the details of the velocity profile written, say $u(R) \propto R^\alpha$, have no implication on the mechanism we discuss in the following as long as $\alpha > -\frac{1}{2}$.

Introducing the local relative curvature $\epsilon = \kappa_\theta h/2$ which is the ratio of the half-sheet thickness to the median line radius of curvature, and is by definition in the range $0 < |\epsilon| < 1$, equilibrium (3.1) has the simplified form

$$P_h - \frac{4\epsilon}{1-\epsilon^2} + We \ln\left(\frac{1+\epsilon}{1-\epsilon}\right) = 0 \tag{3.3}$$

where this time

$$We = \frac{\rho h u^2}{\sigma} \tag{3.4}$$

is the local Weber number built on the sheet thickness h (which is not to be confused with the jet Weber number $We_0 = \rho d_0 u_0^2/\sigma$) and the dimensionless pressure is $P_h = h\Delta p/\sigma$. In the usual limit of an infinitesimal thickness h, that is to say when $\epsilon \ll 1$ equivalent to $\kappa_\theta h \ll 1$, (2.4) is recovered: the curvature only depends on the local Weber number and on the pressure difference according to $\kappa_\theta = -\partial_s \theta = -\Delta p/(We-2)\sigma$.

For a finite thickness, however, several curvatures may be solutions of (3.3) depending on the couple of parameters $\{We, P_h\}$. The critical Weber number $We_c = 2$ marks a bifurcation of the system. Indeed considering $P_h(\epsilon, We)$ compatible with (3.3) one sees that:

(*a*) for $We < We_c$, the pressure P_h evolves monotonically with relative curvature ϵ implying a unique solution;

(*b*) for $We > We_c$, the derivative $\partial_\epsilon P_h$ has two roots revealing a decreasing portion of P_h with ϵ, and three distinct curvatures may verify the normal forces equilibrium.

Figure 7 represents $P_h(\epsilon, We)$ compatible with (3.3) and illustrates this transition. Note that the Weber number $We_c = 2$ corresponds to a velocity u equal to $V = \sqrt{2\sigma/\rho h}$ which, as already mentioned in the introduction, is both the group velocity of long sinuous capillary waves and the Culick–Taylor receding velocity of a free film edge. Therefore, We_c is also critical with respect to both capillary waves and the growth of a hole.

The cause of the multiplicity of solutions is easily understood from the equilibrium in (3.1). It involves an inertial centrifugal term $\rho u^2/R$ where R takes all values between the radii R_i and R_e of internal and external interfaces, respectively, and two centripetal surface tension terms $-\sigma/R_i$ and $-\sigma/R_e$. The sum of those terms must be equal to P_h. For large Weber numbers, the inertial term dominates the capillary term as long as $R_i \simeq R_e \simeq R$. One obtains a first solution of small thickness, that coincides with the usual unique solution when the thickness is infinitesimal. However, one should note that even for large Weber numbers, it is always possible to find an internal radius R_i that is small enough to make the capillary term σ/R_i dominant (as long as the velocity profile is locally like $u(R) \propto R^\alpha$ with $\alpha > -1/2$, which is the case here) and one thus obtains two more solutions, one for each curvature sign.

Let us moreover stress that not all of these solutions are locally stable. The dependency on the radius R of the forces at play being proportional to R^{-1}, their absolute variation $\partial_R R^{-1}$ is negative and centrifugal terms are thus stabilizing while centripetal terms are destabilizing. Considering, for instance, a perturbation of the equilibrium relative curvature ϵ, everything else being kept constant, the stability

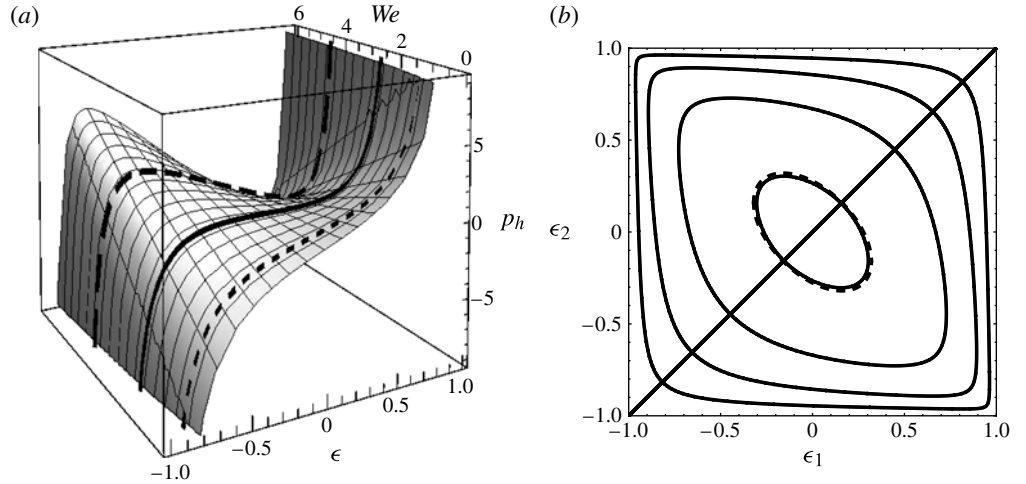

FIGURE 7. (*a*) Pressure P_h solution of (3.3) as a function of We and ϵ. From the bifurcation point $We = We_c = 2$ (plain line) three distinct curvatures may correspond to a given pressure P_h. (*b*) Numerical solutions $\{\epsilon_1, \epsilon_2\}$ of (4.1) (dots) for four values of the local Weber number: $We = 2.1$, 3, 5 and 10 from centre to periphery, respectively. The dashed curve is the ellipse parametrized in (4.4) and plotted for $We = 2.1$.

condition can be written as

$$\left.\frac{\partial P_h}{\partial \epsilon}\right|_{h,We} < 0. \tag{3.5}$$

For large Weber numbers, usual solutions with small curvatures are thus locally stable while solutions with large curvatures are unstable. For $We < We_c$ the unique solution is always locally unstable. This explains the fragility of the crumpled bells, a fact notoriously clear from experiments, which are delicate for this reason.

4. Folds: a free hydraulic jump

4.1. *A simple inflection model*

We now explain the physics behind the sudden inflection of the profile at the fold on hand of a minimal model (which we sophisticate slightly in § 4.2) relying on the previous idea that a thick liquid sheet has several admissible curvatures. Let us consider a curved liquid sheet portion labelled ① of given thickness h_1, local Weber number $We_1 = \rho h u_1/\sigma$ and sustaining a dimensionless pressure difference P_{h_1} between its two interfaces. Its curvature $\kappa_{\theta 1}$ is necessarily a solution of (3.3). Let us wonder whether the adjacent downstream sheet portion ②, which sustains the same pressure difference, may adopt a curvature κ_{θ_2} that is different from $\kappa_{\theta 1}$ (as in figure 8 for instance).

The simplest idea to begin with for this minimal model is to suppose that the liquid velocity is not modified at the transition between both portions, that is to say $u_2 = u_1 = u$. We are here seeking steady solutions and continuity equation thus implies $h_2 = h_1 = h$. As a consequence, $We_2 = We_1 = We$ and $P_{h_2} = P_{h_1} = P_h$. The problem thus amounts, as previously, to look for solutions of (3.3). If ϵ_1 and ϵ_2 are two of these

solutions, they verify

$$-\frac{4\epsilon_1}{1-\epsilon_1^2}+We\ln\left(\frac{1+\epsilon_1}{1-\epsilon_1}\right)=-\frac{4\epsilon_2}{1-\epsilon_2^2}+We\ln\left(\frac{1+\epsilon_2}{1-\epsilon_2}\right). \tag{4.1}$$

For a Weber number that is only slightly larger than the critical number $We_c=2$, one expects that the multiple solutions have small relative curvatures, that is to say $|\epsilon_i|\ll 1$ (this assertion will be verified *a posteriori*). Equation (4.1) can then be written as

$$\begin{cases}\epsilon_1^3+\mathscr{W}\epsilon_1\simeq\epsilon_2^3+\mathscr{W}\epsilon_2\\ \text{with }\mathscr{W}=\dfrac{We-2}{We/3-2}\end{cases} \tag{4.2}$$

whose approximation obviously still accepts the trivial solution $\epsilon_2=\epsilon_1$. This approximation is valid for $|\mathscr{W}|\ll 1$ that is to say for We close to 2. For a given curvature $\epsilon_1\ll 1$, two further solutions are

$$\epsilon_2=\frac{-\epsilon_1\pm\sqrt{-4\mathscr{W}-3\epsilon_1^2}}{2}. \tag{4.3}$$

These solutions fall on an ellipse in the $\{\epsilon_1,\epsilon_2\}$ space

$$\frac{(\epsilon_1+\epsilon_2)^2}{4}+\frac{3\,(\epsilon_1-\epsilon_2)^2}{4}=-\mathscr{W}. \tag{4.4}$$

Its major axis is oriented along the bisector plane $\{-1,1\}$ and its extremal radii are $\sqrt{-4\mathscr{W}/3}$ and $\sqrt{-4\mathscr{W}}$.

Figure 7 shows the couples $\{\epsilon_1,\epsilon_2\}$ obtained from the numerical solution of (4.1) for various Weber numbers. For We close to We_c, multiple solutions have small relative curvatures and the ellipse of (4.4) is a good approximation. For larger We, however, even for an initial curvature $|\epsilon_1|\ll 1$, curvatures $|\epsilon_2|$ that are compatible and non-trivial are of order one; that is to say the radius of curvature R_i of their internal interface tends to 0.

If we want to explain the bell profile inflection by the sudden transition from a given positive to a negative curvature, we must make sure that this transition may occur spontaneously, that is to say that the energy level corresponding to the second curvature is lower than that corresponding to the first. This level is the sum of the kinetic and the pressure potential energy fluxes transported by the liquid sheet and can be written as

$$\begin{cases}E=\displaystyle\int_{R_m-(h/2)}^{R_m+(h/2)}\left(\frac{\rho u^2}{2}+p\right)u\,\mathrm{d}R\\ \text{where }p=p_i-\dfrac{\sigma}{R_m-\dfrac{h}{2}}+\rho u^2\ln\left(\dfrac{R}{R_m-\dfrac{h}{2}}\right).\end{cases} \tag{4.5}$$

It does not involve the surface energy associated with σ since the flow being steady, there is no surface creation. In terms of the variables we adopted it becomes

$$\frac{E}{\sigma u}=\frac{We}{2\epsilon}\left[(1+\epsilon)\ln\left(\frac{1+\epsilon}{1-\epsilon}\right)-\epsilon\right]-\frac{2\epsilon}{1-\epsilon}+\frac{p_i h}{\sigma} \tag{4.6}$$

which can be transformed, with the aid of (3.3), into the more useful expression

$$\frac{E}{\sigma u} = 2 - \frac{We}{2} - \frac{p_i - p_e}{\sigma}\frac{h}{2} - \frac{p_i - p_e}{\sigma}R$$
$$= \mathscr{C}(We, h) - \frac{p_i - p_e}{\sigma}R \tag{4.7}$$

where $\mathscr{C}$ is a quantity conserved between the various solutions since both the Weber number and the thickness are conserved in this minimal model. It then appears that for a pressurized bell, i.e. when $\Delta p = p_i - p_e > 0$, the transition from a negative curvature, i.e. whose curvature centre is exterior to the bell, to a positive curvature corresponds to an energy loss since $\Delta E = E_2 - E_1 \sim -u\Delta pR$ is negative.

The inflection at the fold is thus associated with an energy dissipation at the transition from a local negative curvature to a positive curvature. The first dissipation mechanism we can imagine is that due to the sheet internal shear associated with the flow along the sharp curvatures at the fold. Still considering a uniform velocity profile $\boldsymbol{u} = u\boldsymbol{e}_\theta$ in a transverse cross-section, the dissipation rate per unit volume $\frac{1}{2}\eta(\boldsymbol{\nabla u} + \boldsymbol{\nabla u}^{\mathrm{T}}) : (\boldsymbol{\nabla u} + \boldsymbol{\nabla u}^{\mathrm{T}})$ can be written as $\eta\,(u/R)^2$ where η is the dynamical viscosity of the liquid. Integrated over the sheet thickness, and for a turning angle $\Delta\theta$, the dissipated power is

$$E_\eta = \eta u^2 \ln\left(\frac{1+\epsilon}{1-\epsilon}\right)\Delta\theta = \eta u^2 \ln\left(\frac{R_m + \frac{h}{2}}{R_m - \frac{h}{2}}\right)\Delta\theta. \tag{4.8}$$

For instance, for the bell in figure 5 the velocity is $u = 2.36$ m s^{-1}, the thickness at the fold estimated from (2.1) is $h = 25$ μm, the pressure difference is $\Delta p = 3.2$ Pa and the smallest radius of curvature we have been able to measure is $R \sim 100$ μm. Considering that dissipation occurs over an angle $\Delta\theta$ of order unity we get

$$E_\eta \sim -\Delta E \approx 10^{-3}\ \mathrm{W\,m^{-1}}. \tag{4.9}$$

This estimate of the viscous dissipation is indeed of the same order of magnitude as the energy difference required to transit from one curvature solution to the other, suggesting that the former is likely to explain the existence of crumpled bells whose profiles have a stationary dissipating inflection point at the fold.

4.2. *A more refined description: the free hydraulic jump*

One can object to the previous sketch on the grounds that it does not verify momentum conservation between portions ① and ② of opposite curvatures. In this section we present a more complete, but also slightly more complex way of studying the possibility of a profile inflection that notably also accounts for the flow regime change at the fold.

We picture this inflection as a sudden jump, in a way totally analogous to the classical hydraulic jump treatment (Lord Rayleigh 1914), with however some necessary generalizations. The first is that the transverse pressure gradient is no longer resulting from a constant gravity term ρg but from a centrifugal term $\rho u^2/R$ depending both on the local velocity and curvature; the second is that the sheet is freely suspended and so both interfaces positions may vary at the jump. This imposes that we determine not only a change in the thickness h but also a possible offset of the median lines that we call X (see figure 8). As we will see, the introduction of the offset X is also required by the conservation of the angular momentum across the suspended jump.

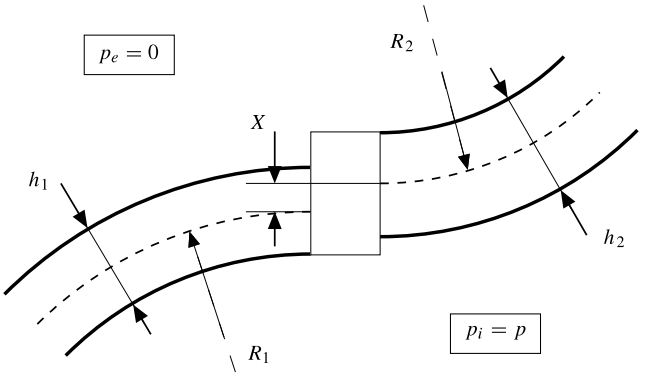

FIGURE 8. Sketch of the hydraulic jump on a freely suspended sheet.

To summarize, we seek for the conditions u_2, h_2 and R_{m2} immediately downstream of the jump and for the offset X and pressure difference Δp, that are compatible with given initial conditions u_1, h_1 and R_{m1}. The five unknown variables are constrained by three conservation equations across the jump, namely that of mass, tangential linear momentum and angular momentum, and two equations (3.3) for the normal linear momentum insuring the compatibility of conditions in ① and ② with Δp.

4.3. *The system of equations*

(*a*) Momentum conservations projected on $\boldsymbol{e}_n$ that we already established in (3.3) can be written as

$$\frac{\Delta p}{\sigma} 2\epsilon_i R_{mi} - \frac{4\epsilon_i}{1-\epsilon_i^2} + We_i \ln\left(\frac{1+\epsilon_i}{1-\epsilon_i}\right) = 0 \tag{4.10}$$

where the index i takes, here like everywhere hereafter, the values 1 and 2 in the domains ① and ②, respectively.

(*b*) Mass conservation across the jump is

$$\begin{cases} q_1 = q_2 \\ q_i = \displaystyle\int_{R_{mi}-(h_i/2)}^{R_{mi}+(h_i/2)} \rho u_i \, \mathrm{d}R \end{cases} \tag{4.11}$$

which can also be written in the following way in terms of the variables we adopted

$$We_1 \epsilon_1 R_{m1} = We_2 \epsilon_2 R_{m2}. \tag{4.12}$$

(*c*) Momentum conservation along $\boldsymbol{e}_\theta$ requires

$$\begin{cases} Q_1 + \Delta p \left(\dfrac{h_2 - h_1}{2} - X\right) = Q_2 \\ Q_i = \rho u_i^2 h_i + \displaystyle\int_{R_{mi}-(h_i/2)}^{R_{mi}+(h_i/2)} p(R) \, \mathrm{d}R - 2\sigma \end{cases} \tag{4.13}$$

where Q_i is the sum of the momentum flux and the stresses applying on each sheet cross-section i, and the term involving Δp accounts for the air pressure on the non-aligned portions of both cross-sections (see figure 8). Equation (4.13) can similarly be

written as

$$\frac{\Delta p}{\sigma}(\epsilon_1 R_{m1} - X) - \frac{2}{1-\epsilon_1} + We_1 \frac{1+\epsilon_1}{2\epsilon_1} \ln\left(\frac{1+\epsilon_1}{1-\epsilon_1}\right) = \frac{\Delta p}{\sigma}\epsilon_2 R_{m2} - \frac{2}{1-\epsilon_2} + We_2 \frac{1+\epsilon_2}{2\epsilon_2} \ln\left(\frac{1+\epsilon_2}{1-\epsilon_2}\right). \tag{4.14}$$

(d) Finally angular momentum conservation along the joint normal to $\boldsymbol{e}_n$ and $\boldsymbol{e}_\theta$ leads to

$$\begin{cases} \mathscr{C}_{1/M_1} - \dfrac{\Delta p}{2}\left[\left(\dfrac{h_2}{2} - X\right)^2 - \left(\dfrac{h_1}{2}\right)^2\right] = \mathscr{C}_{2/M_2} + X\,Q_2 \\ \mathscr{C}_{i/M_i} = \displaystyle\int_{R_{mi}-(h_i/2)}^{R_{mi}+(h_i/2)} (R - R_{mi})\, p(R)\, \mathrm{d}R \end{cases} \tag{4.15}$$

where $\mathscr{C}_{i/M_i}$ is the angular moment associated with the pressure in the cross-section i (contributions of liquid momentum flux and surface tension are both nil) around the point M_i situated at mid-thickness of the sheet, and the term involving Δp again accounts for the influence of air pressure on the non-aligned portions of both cross-sections. Equation (4.15) can equivalently be written

$$\frac{\Delta p}{2\sigma}(\epsilon_1 R_{m1})^2 + \frac{We_1 R_{m1}}{2\epsilon_1}\left[\epsilon_1 - \frac{1-\epsilon_1^2}{2}\ln\left(\frac{1+\epsilon_1}{1-\epsilon_1}\right)\right] = \frac{\Delta p}{2\sigma}(\epsilon_2 R_{m2} - X)^2 + \frac{We_2 R_{m2}}{2\epsilon_2}\left[\epsilon_2 - \frac{1-\epsilon_2^2}{2}\ln\left(\frac{1+\epsilon_2}{1-\epsilon_2}\right)\right] + X\frac{Q_2}{\sigma} \tag{4.16}$$

with

$$\frac{Q_2}{\sigma} = \frac{\Delta p}{\sigma} 2\epsilon_2 R_{m2} - \frac{2}{1-\epsilon_2} + We_2 \frac{1+\epsilon_2}{2\epsilon_2} \ln\left(\frac{1+\epsilon_2}{1-\epsilon_2}\right). \tag{4.17}$$

4.4. *Resolution*

We are in possession of a system of five equations namely (4.10) for ① and ②, (4.11), (4.13) and (4.15). We make it dimensionless with $h_1 = 2\,\epsilon_1 R_{1m}$, σ and ρ. The only remaining variables are then We_1 and ϵ_1 that we will consider as our two control parameters and the five unknown variables Δp, R_{2m}, We_2, ϵ_2 and X. The system may look at first sight heavy but it is possible to solve it almost completely analytically. We detail below the key steps leading to the result.

The expression for We_2 in terms of the other variables is straightforward from mass conservation, and that of R_{m2} and X derives from (4.14) and (4.16) used jointly with (4.10) (those manipulations obviously assume that $0 < |\epsilon_i| < 1$, which corresponds to the range where we seek non-trivial solutions. Similarly the radii R_{mi} are considered finite)

$$\begin{cases} R_{m2} = R_{m1} + X \\ We_2 = \dfrac{\epsilon_1 R_{m1}}{\epsilon_2 R_{m2}} We_1 \\ X = \dfrac{We_1}{2}\left(\dfrac{\epsilon_1}{\epsilon_2} - 1\right) R_{m1}. \end{cases} \tag{4.18}$$

One therefore only needs to equate downstream and upstream pressure differences with the aid of (4.10) to reduce the system to an equation of the unique variable ϵ_2

that is analogous to (4.1)

$$\frac{1}{\epsilon_1 R_{m1}}\left[\frac{4\epsilon_1}{1-\epsilon_1^2} - We_1 \ln\left(\frac{1+\epsilon_1}{1-\epsilon_1}\right)\right] = \frac{1}{\epsilon_2 R_{m2}}\left[\frac{4\epsilon_2}{1-\epsilon_2^2} - We_2 \ln\left(\frac{1+\epsilon_2}{1-\epsilon_2}\right)\right] \quad (4.19)$$

where R_{m2} and We_2 can be expressed from expression (4.18). This rational, logarithmic equation is highly nonlinear, and does not present any obvious solution except for $\epsilon_2 = \epsilon_1$. We therefore seek solutions in the case $|\epsilon_1| \sim |\epsilon_2| \ll 1$ and $We_1 \sim 2$ which corresponds to the conditions around the fold. Writing $\epsilon_2 = y\epsilon_1$, where $|y| \sim 1$, (4.10) developed in power series of ϵ_1 can be written as

$$2(We_1 - 2)\frac{[We_1(y-1) - 4y](y-1)}{[We_1(y-1) - 2y]^2}\epsilon_1 + O(\epsilon_1^3) = 0 \quad (4.20)$$

whose relevant solution at the first order is

$$y = -\frac{We_1}{4 - We_1}. \quad (4.21)$$

The conditions immediately downstream of the jump are thus as follows

$$\begin{cases} R_{m2} = -R_{m1} = \dfrac{X}{2} \\ We_2 = 4 - We_1 \\ \epsilon_2 = -\dfrac{We_1}{4 - We_1}\epsilon_1. \end{cases} \quad (4.22)$$

It must be noticed first that the curvature reverses at the jump (as one sees at the crumpled bells folds), and second that if the Weber number is larger than 2 upstream, i.e. if $We_1 > We_c$, it is then smaller than 2 downstream, i.e. $We_2 < We_c$. The inflection is thus actually a hydraulic jump across which the flow transits from a supercritical regime (with respect to capillary wave propagating at the Taylor–Culick velocity $V = \sqrt{2\sigma/\rho h}$) upstream from the jump to a subcritical regime downstream. This is however a new type of capillary jump since:

(*a*) the liquid sheet is suspended and therefore, as already mentioned, both interfaces are free to move;

(*b*) the capillary pressure associated with the curvature of each interface plays a role; and

(*c*) the transverse pressure gradient is not gravity induced, but is rather induced by the centripetal acceleration of the fluid as it flows along the highly curved bell profile.

This also explains why the crumpled bell in figure 9 becomes 'rough' as the jump appears, and only downstream from it: sinuous perturbations have a group velocity $V > u$ and are able to propagate upwards against the flow up to the fold where they become stationary and accumulate until they dissipate, by contrast with the jump upstream region where perturbations are advected through the fold.

The last equation of system (4.19) has also been solved numerically without using the approximation $|\epsilon_1| \ll 1$. The solution couples $\{\epsilon_1, \epsilon_2\}$ are plotted in figure 10 and coincide with the expression (4.22) we derived for small curvatures.

4.5. *Comparison with experiments*

The results of the previous section can be confronted with experiments using the bell profile of figure 5. The initial jet diameter d_0 is known with a 1 % relative precision while the mass flow rate is measured by weighting with a 0.1 % relative

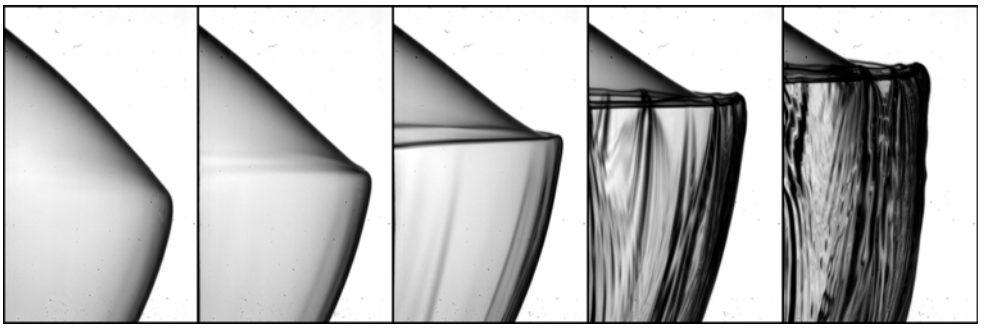

FIGURE 9. Sudden onset of a stable fold at the maximal radius of a bell when the jet flow rate is progressively decreased, which is equivalent to a progressive increase of the dimensionless pressure P. The fold forms as the reversing condition $P > P_c$ is verified for the first time and the liquid sheet, initially smooth over its whole surface, becomes 'rough' over its downstream portion.

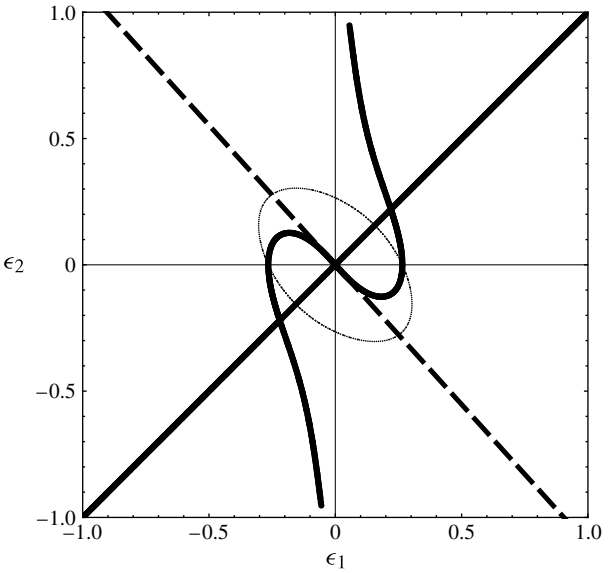

FIGURE 10. Numerical solutions $\{\epsilon_1, \epsilon_2\}$ of (4.19) (dots) for a local Weber number $We_1 = 2.1$. The dashed slanted line represents the asymptotical solution (4.22) for small ϵ_1 and ϵ_2. For comparison the small dots represent the couples solution of (4.1).

precision. Pressure is the only parameter that is not measured directly, but it can be estimated very precisely (around 1 % of relative precision) by looking for the solution of (2.4) that best fits the experimental profile, in the very same way surface tension of a liquid can be measured through the shape of a pendant drop. It is precisely for this high susceptibility of the bell shape on its internal pressure that Brunet *et al.* (2004) suggested the use of closed liquid bells pressurized at a value close to P_c as a precision barometer. The fit gives $P = 0.96$ which corresponds to a pressure difference $\Delta p = 3.2$ Pa. Note that it is of the same order as the limit pressure given by (2.11) $P_c = 0.82$, above which a profile loop is expected in the absence of gravity. The fact that gravity allows for a slightly larger pressure is also consistent since in

our experimental set-up, the action of gravity is opposed to that of an internal excess pressure all the way down to the possible loop (see figure 4).

The situation as it can be observed immediately upstream of the fold is the following: taking the interior as the reference, the pressure Δp is positive and the radius of curvature $R_{1m} = \kappa_{\theta 1}^{-1}$ is negative. If we moreover suppose that the numerical profile is faithful to the experiment until the immediate neighbourhood of the jump, we can estimate the conditions there from this numerical profile at its maximal radial extension, that is to say just before it loops in $\theta = \pi$. The local Weber number, the thickness and the radius of curvature are then respectively found to be $We_1 = 2.05$, $h_1 = 25$ μm and $R_{m1} = \kappa_{\theta 1}^{-1} = -1$ mm according to this method. Note that this evaluation concerning the curvature *before* the jump is not contradictory with the minimal value $R_m \sim 100$ μm we used for the estimate of E_η in (4.9) corresponding to the curvature at the jump that realizes both the offset X and the energy dissipation E_η. One sees that $\epsilon_1 = h_1/(2R_{m1}) \sim 1/80 \ll 1$ and (4.21) and (4.22) can thus reasonably be used. In that context, the excess pressure can be expressed from the solutions of (4.22) as a power series in ϵ_1 according to

$$\Delta p = -\frac{\sigma\,(We_1 - 2)}{R_{m1}} + O(\varepsilon_1^2). \tag{4.23}$$

Let us emphasize two points: first, the jump forms in the conditions expected by theory, which imposes that the sign of $\Delta p R_{1m}$ be negative, when $We_1 > 2$, for an hydraulic jump to occur; second, for the parameters measured on the bell, the excess pressure liable to trigger the jump is $\Delta p = 3.5$ Pa according to (4.23) and it is very close to the value $\Delta p = 3.2$ Pa measured by fitting the profile.

Finally, in the same way we did before in § 4.1, it is necessary to make sure that the jump actually corresponds to a flow dissipation since it happens in experiments spontaneously without any external input. Using the solutions of system (4.22), the dissipated power, expressed by the energy flux difference established in (4.6) (where this time we have to consider $u_1 \neq u_2$) becomes

$$E_1 - E_2 = 4\sigma u_1 \frac{We_1 - 2}{We_1} + O(\varepsilon_1^2) \tag{4.24}$$

which simply means that across the hydraulic jump, transiting from the supercritical regime $We_1 > 2$ to the subcritical regime $We_2 < 2$, the energy flux is partially dissipated, in the very same way the head pressure of a river decreases at the hydraulic jump connecting the torrential to the fluvial regime.

To summarize, the capillary hydraulic jump as we have described it accounts for all of the observations we made on the bells presenting a double inflection.

(*a*) It may happen in a stationary flow, and corresponds to an energy dissipation $E_2 < E_1$.

(*b*) Considering the values of the pressure difference Δp and of the injection Weber number We_0 of such bells, it is expected that it happens in the neighbourhood of the bell maximal radial extension L at a location where the *local* Weber number We is close to but larger than 2.

(*c*) It may happen only when the pressure is smaller on the side of the local concavity of the sheet than on the opposite side, as it actually is immediately upstream from the crumpled bells fold ($\kappa_\theta \Delta p < 0$).

(*d*) The two former conditions are only met for bells whose internal pressure is positive and exceeds the threshold condition $P > P_c$ by a very small amount.

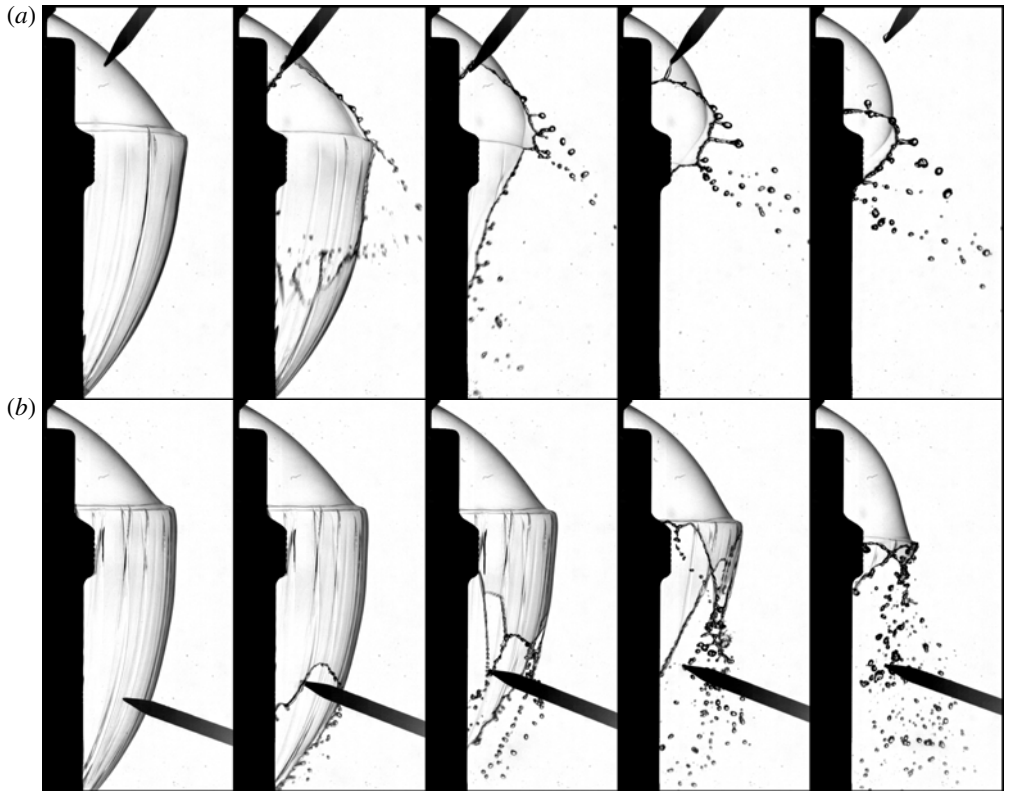

FIGURE 11. Puncture of a crumpled bell. (*a*) The hole is initiated upstream of the fold and its border does not recede against the flow, i.e. $V < u$ or equivalently $2 < We$. The flow is supercritical and the stationary border locally forms a Mach cone. (*b*) The hole is initiated downstream of the fold and its border recedes against the stream ($V > u$ or $2 > We$), thus revealing a subcritical flow.

(*e*) For such bells, the hydraulic jump occurs and it induces a sharp profile inflection ($R_{m1}R_{m2} < 0$) together with a discontinuity in alignment towards the inside of the bell ($X > 0$).

(*f*) Downstream of the jump, the local Weber number is smaller than 2 and corresponds to a subcritical flow, consistent with the bells 'blurred' aspect in this region.

Finally, the subcriticality of the flow can be checked experimentally by puncturing the bell as in figure 11. In the period immediately following the puncture, when the pressurized air cavity has not yet escaped through the growing hole, the bell shape remains globally unchanged. One then sees that:

(*a*) the border of a hole triggered just upstream of the fold is advected by the flow as is expected for an usual supercritical liquid sheet since $We_1 > 2$ is equivalent to $u_1 > V_1 \equiv \sqrt{2\sigma/\rho h_1}$;

(*b*) the border of a hole triggered just downstream of the fold recedes against the flow, demonstrating that $u_2 < V_2 \equiv \sqrt{2\sigma/\rho h_2}$ which is equivalent to $We_2 < 2$ as suits to a subcritical flow.

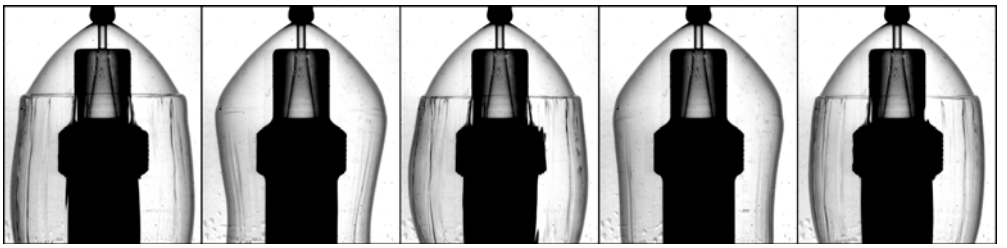

FIGURE 12. Natural periodic oscillations of a bell formed under conditions close to those leading to a stationary crumpled shape. The regular repeated apparition and disappearing of the fold visible as an horizontal line illustrate the link between fold and wrinkles: when the fold forms (as in the first, third and fifth images) the wrinkles develop; when the fold disappears (as in the second and fourth images) the wrinkles vanish.

5. Liquid sheet wrinkles

Downstream from the hydraulic jump, crumpled bells are not only rough but also develop vertical wrinkles that are regularly spaced around the symmetry axis, as one sees in figures 9, 11 and 12. Those wrinkles correspond to portions of the sheet with a larger thickness, forming in response to the acceleration the liquid experiences as it flows along the curved profile of the bell. We discuss now why the wrinkles appear suddenly at the fold, or also alternatively at the extreme downstream location where the sheet has contracted and almost meets the axis.

5.1. *Observations*

As figure 9 illustrates, the onset of wrinkles is closely related with that of the profile double inflection characterizing the hydraulic jump. This link is further emphasized in figure 12 which shows a bell formed under conditions that are very close to those triggering a hydraulic jump. Fortuitously, this bell oscillates at a low frequency between a globally convex shape and a shape presenting a fold, thus providing an opportunity to test the causality between the occurrence of a fold, and wrinkles. Two oscillation periods are presented in figure 12, and at every formation of the fold wrinkles develop, to subsequently vanish as the profile becomes convex again.

The origin of those wrinkles is suggested by the strong centrifugation events one observes once in a while at the fold: a ligament forms at the external interface, then stretches and subsequently pinches to eject a drop (see figure 13). Such events illustrate the strong normal acceleration $\kappa_\theta u^2$, of order 10^3 m s^{-2}, the fluid particles experience as they flow along the bell profile, particularly in regions of high curvature, like at the fold. We argue that this acceleration is the source of the sheet destabilization which generates the thickness modulations we observe.

The wrinkles are globally stationary structures but they are not frozen. They appear and disappear regularly. However, those reorganizations permanently maintain a regular spacing between the wrinkles suggesting that a particular wavelength λ is selected by the system. The observation of a bell under monochromatic lighting allows the visualization of the thickness modulations development (see figure 14). The iso-thickness lines reveal that the thickness maxima (in the azimuthal direction) are on the same radii as the wrinkles visible immediately downstream of the fold. This observation emphasizes that the mode selection occurs just upstream from the fold and that the growth of the wrinkles amplitude continues all along the fold.

Finally, we note that the wavelength λ is of the order of 1 cm for a sheet thickness $h \sim 10$–100 μm at the maximal bell radial extension, leading to a large ratio $\lambda/h \gg 1$. We consider the above-listed observations in the next section.

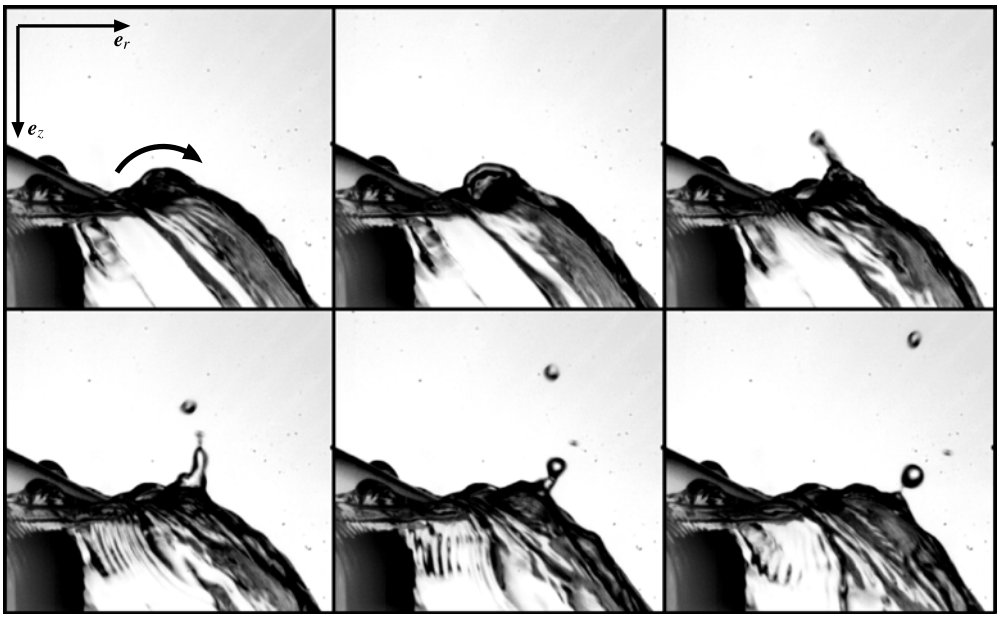

FIGURE 13. Illustration of the acceleration the liquid experiences as it flows along the fold profile (in the direction indicated by the arrow): the liquid crest destabilizes and a centrifuged ligament is ejected which subsequently fragments.

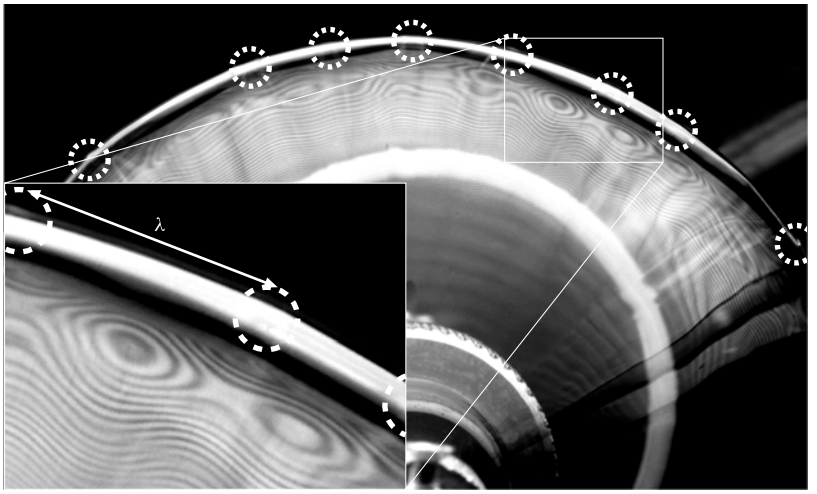

FIGURE 14. Top view of a crumpled bell under the monochromatic lighting of a sodium lamp at 589 nm (the beat between both frequencies of the doublet is not visible here). The bell axis is bottom centred and a zoom is presented in the inset. Interferences show the liquid sheet iso-thickness lines and reveal the azimuthal thickness modulations that form immediately upstream of the fold. Note that the latter coincide with the wrinkles (circled by a dashed white line) that develop markedly at the fold only.

5.2. *Growth along the bell profile*

The centripetal acceleration $\gamma = \kappa_\theta u^2$ the liquid experiences promotes the inertial destabilization of the interfaces all along the bell profile. The development of this

instability, of a Rayleigh–Taylor type, depends on the local conditions. For any sheet of thickness h, the growth rate associated with a wavenumber $k = 2\pi/\lambda$ writes (Keller & Kolodner 1954; Bremond & Villermaux 2005)

$$s(k, h, \gamma) = \omega \left\{ \left(\frac{k}{k_c}\right)^3 \left[\coth(kh) - \sqrt{\operatorname{csch}^2(kh) + \left(\frac{k_c}{k}\right)^4} \right] \right\}^{1/2} \tag{5.1}$$

where $k_c = \sqrt{\rho|\gamma|/\sigma}$ is the critical wavenumber, and $\omega = (\rho|\gamma|^3/\sigma)^{1/4}$ the characteristic growth rate in the usual infinite thickness limit, i.e. $k_c h \to \infty$.

Let us now determine the most amplified mode between two points of the bell profile parametrized by θ_i and θ_f, respectively. For that purpose we give the discussion in terms of the spatial variations with respect to the local sheet normal orientation θ straightforwardly related to the temporal variation via $\mathrm{d}\theta = \kappa_\theta u \, \mathrm{d}t$. We need to account on the one hand for the spatial growth rate

$$\mathfrak{s} = s \times \frac{1}{\kappa_\theta u} \tag{5.2}$$

of the mode we consider, but also on the other hand for the modulation of its associated amplitude and for the wavenumber drift due to the transverse spatial stretching rate

$$\mathfrak{e}_\perp = \frac{1}{r}\frac{\partial \boldsymbol{u}}{\partial \phi} \cdot \boldsymbol{e}_\phi \times \frac{1}{\kappa_\theta u} \tag{5.3}$$

in the azimuthal direction $\boldsymbol{e}_\phi$, that is to say in the direction parallel to the instability wavenumber $\boldsymbol{k}$.

The local growth rate s is here small with respect to the characteristic evolution time of the substrate experienced by a liquid sheet portion in its motion. Considering an azimuthal mode $A\exp(\mathrm{i}k_i r\phi)$, its gain $\mathscr{A}(\theta_i, \theta_f, k_i) = \ln[A(k_f, \theta_f)/A(k_i, \theta_i)]$ between coordinates θ_i and θ_f can then be written as the product of the successive infinitesimal growths

$$\begin{cases} \mathscr{A}(\theta_i, \theta_f, k_i) = \displaystyle\int_{\theta_i}^{\theta_f} [\mathfrak{s}(k, h, \gamma) - \mathfrak{e}_\perp] \, \mathrm{d}\theta \\ \text{with } k(\theta) = \left(\displaystyle\int_{\theta_i}^{\theta_f} \mathfrak{e}_\perp \, \mathrm{d}\theta \right)^{-1} \times k_i. \end{cases} \tag{5.4}$$

In the case of a Savart bell there is no longitudinal stretching since $\partial_r u = 0$, and the contribution of the azimuthal stretching can then be directly written in terms of the thickness evolution according to

$$\mathfrak{e}_\perp = -\frac{\mathrm{d}\ln h}{\mathrm{d}\theta} \tag{5.5}$$

which is equivalent to $\mathrm{d}(kh) = 0$. Equation (5.4) therefore simplifies into

$$\begin{cases} \mathscr{A}(\theta_i, \theta_f, k_i) = \displaystyle\int_{\theta_i}^{\theta_f} \mathfrak{s}(k, h, \gamma) \, \mathrm{d}\theta + \ln\left(\frac{h_f}{h_i}\right) \\ \text{with } k = \dfrac{h_i}{h} \times k_i. \end{cases} \tag{5.6}$$

Moreover, all along the bell profile thickness h, velocity u and local curvature κ_θ are not arbitrary, but are related to each other by the bell equilibrium condition.

For the sake of clarity, we only consider in the following the case of large Bond numbers for which this equilibrium amounts to (2.5) (one does not expect that the physics of the phenomenon be modified for realistic Bond numbers, but the associated complications would however necessarily prevent any analytical description). The parameter $k_c h = \sqrt{\rho|\gamma|h^2/\sigma}$ which determines the shape of the local dispersion equation (5.1) can then be written as

$$k_c h = \frac{8}{We_0}\frac{1}{r}\sqrt{\frac{|\cos\theta - Pr|}{1-r}}. \tag{5.7}$$

One sees that $k_c h$ decreases with r on a first portion of the bell profile and then increases up to the maximal extension. It is therefore everywhere smaller than the extremal values. The first one, at the jet, is

$$k_c h|_{r=d_0/L} \simeq \frac{1}{2}\sqrt{|\cos\theta_0 - Pr_0|} < \frac{\sqrt{|\cos\theta_0|}}{2} < \frac{1}{2} \tag{5.8}$$

where we have considered $d_0 \ll L$. The second can be written as

$$k_c h|_{r=r_m\sim 1} \simeq \frac{8}{We_0}\sqrt{\frac{|\cos\theta - P|}{1-r_m}} < \frac{8\sqrt{2}}{We_0}\sqrt{\frac{1}{1-r_m}} \tag{5.9}$$

and strongly depends on the maximal extension value r_m. This latter one is close to unity (the absolute limit by definition) only when the pressure P is close to the reversing critical pressure P_c, and in that case (5.9) can be transformed into

$$\begin{cases} k_c h|_{r=r_m} \simeq \dfrac{16}{We_0}\sqrt{\dfrac{1-P}{P_c - P}} & \text{when } P < P_c \\ k_c h|_{r=r_m} \simeq \dfrac{16}{We_0}\sqrt{\dfrac{1+P}{P - P_c}} & \text{when } P > P_c. \end{cases} \tag{5.10}$$

It therefore appears that $k_c h$ is always small with respect to 1, except for the bells whose internal pressure is very close to the critical pressure P_c. This is by definition the case for crumpled bells. However, the more penalizing estimates for all of the bells we observed show that $k_c h$ is always smaller than $1/3$. This condition is not necessarily general but we will use it here to consider only the *thin layer* destabilization regime, that is to say the regime when $k_c h \ll 1$, as the observation of the selected wavelengths of order 10 to 100 the local sheet thickness suggests.

In that limit $k_c h \ll 1$, the temporal growth rate of the most amplified modes intrinsically depends on h according to

$$s_m = \omega\sqrt{\frac{k_c h}{2}}\sqrt{1 - \left(\frac{k}{k_c}\right)^4}. \tag{5.11}$$

Figure 15 illustrates the convergence of the dispersion relation (5.1) towards this limit. It is clear that as soon as the relative thickness is such that $k_c h \leqslant \frac{1}{2}$, the error on the maximal growth rate is smaller than 15 %. We therefore consider in the following that (5.11) offers a good description of the instability growth all along the profile; it is an upper bound of its growth.

The foremost remarkable behaviour in the instability growth when $k_c h \ll 1$ is that the growth rate does no longer depends on the acceleration direction, i.e. on the curvature sign in our case. Indeed both interfaces evolve together and grow at the same rate (Bremond & Villermaux 2005).

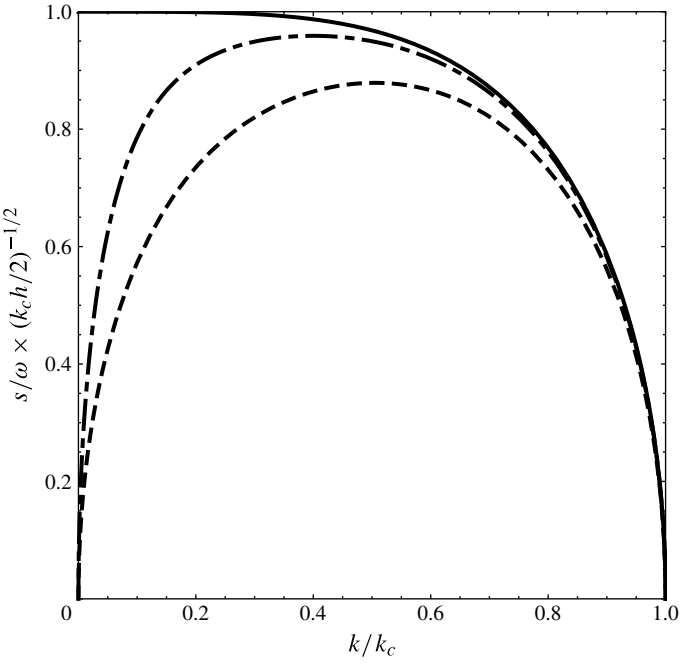

FIGURE 15. Dispersion equation (5.1) for $k_c h = \frac{1}{2}$ (- -), $k_c h = \frac{1}{5}$ (- –) and $k_c h \to 0$ (—). Note the plateau of the limit curve for dimensionless wavenumbers $k/k_c \lesssim \frac{1}{2}$.

Therefore, to the maximal temporal growth rate $s_m = \sqrt{\rho h/2\sigma}|\gamma| = |\gamma|/V$ corresponds a spatial growth rate

$$\mathfrak{s}_m = \frac{|\kappa_\theta u^2|}{V}\frac{1}{\kappa_\theta u} = \sqrt{\frac{We}{2}}\frac{|\mathrm{d}\theta|}{\mathrm{d}\theta} = \frac{1}{\sqrt{r}}\frac{|\mathrm{d}\theta|}{\mathrm{d}\theta}. \tag{5.12}$$

Remarkably, this spatial growth rate is independent of the local curvature. It solely depends on the local Weber number, or equivalently on the radius r for the present case of an axi-symmetrical bell with purely radial flow. The growth rate $\mathfrak{s}_m$ is large when the radius r is small, precisely where the curvature evolves little, leading to a small total growth, but also where the substrate stretching rate which inhibits the instability is the largest. Indeed, this spatial stretching rate can be written as

$$\mathfrak{e}_\perp = -\frac{\sin\theta}{\kappa_\theta r} \tag{5.13}$$

and it is thus large close to the bell axis and negligible in $r \sim 1$. Its sign depends on the hemisphere we consider:

(*a*) on the first hemisphere, where streamlines diverge and impose the stretching inhibiting the instability, the wrinkles growth is limited to radii of order one; this is the reason why wrinkles do not show up upstream from the fold;

(*b*) conversely on the second hemisphere the streamlines convergence combine with the instability growth to amplify the thickness modulations; this explains why, even without a fold, wrinkles are always observed in the vicinity of the axis downstream from the equator.

5.3. *Growth at the fold*

Now that we have clarified why destabilization may not occur before radii r of order one, we will focus in the present section on the development of a perturbation at the fold. In that region the substrate varies very little as $\Delta r/r \ll 1$ so that stretching and wavenumber drift can be neglected. It is therefore possible to express the upper bound net gain $\mathscr{A}_m$ of a mode from the locally most amplified perturbation whose spatial growth rate is $\mathfrak{s}_m$ defined in (5.12)

$$\mathscr{A}_m = \int_{\theta_i}^{\theta_f} \mathfrak{s}_m \mathrm{d}\theta = \int_{\theta_i}^{\theta_f} \sqrt{\frac{We}{2}} |\mathrm{d}\theta| = \int_{\theta_i}^{\theta_f} \frac{1}{\sqrt{r}} |\mathrm{d}\theta|. \tag{5.14}$$

It is obviously possible to integrate (5.6) numerically for any usual bell profile and angles θ_i and θ_f from (2.6) and (2.5) with $h(\theta) = d_0^2/8r$, $u(\theta) = u$, $\kappa_\theta(\theta) = -\partial_s\theta$ and $\gamma(\theta) = \kappa_\theta u^2$. This method always gives smaller gains, but close to those of the approximation (5.14) for the most unstable mode. This is not surprising if one recalls that in the limit $k_c h \ll 1$, the dispersion relation (5.1) does not present a marked maximum at a given wavelength but on the contrary a broad plateau, implying that almost all wavelengths $\lambda > \lambda_c$ grow at the same rate (see figure 15).

Considering now that the local Weber number is close to 2 and almost uniform all over the fold curvatures since $r \simeq 1$, equation (5.14) amounts to the simplest form

$$\mathscr{A}_m \simeq \int_{\theta_i}^{\theta_f} |\mathrm{d}\theta|. \tag{5.15}$$

It simply means that all of the successive curvatures, whether their sign be positive or negative, along which the liquid flows as it follows the fold profile contribute to the growth of the inertial destabilization. As already mentioned, this is a direct consequence of the fact that for large wavelengths (with respect to the thickness) both interfaces couple and grow at the same rate irrespective of the direction of the acceleration.

It is now clear why for a globally similar shape, an integrally convex profile does not present wrinkles while a profile presenting a fold does.

(a) In the former case $\int |\mathrm{d}\theta| = \Delta\theta \sim \pi/2$ (see figure 17).

(b) In the latter case, owing to the double inflection of the profile, $\int |\mathrm{d}\theta| > 3\pi/2$.

This may look at first sight to be a small difference, but the ratio of the two gains $\mathrm{e}^{\pi} > 20$ is certainly large enough to explain that wrinkles are marked in one case and not in the other.

5.4. *Range of unstable wavelengths*

Crumpled bells exist only in the vicinity of a particular condition for the jet deflection angle and internal pressure so that their parameters are by definition hardly tunable. Moreover, we have shown that the mode selection of the wrinkles is global and is therefore conditioned by the history of the curvatures that a liquid portion has experienced in its transit along the bell profile, upstream and in the region of the fold, which makes analytical predictions for the destabilization wavelength λ difficult. This would be of little use anyway since, in the thin sheet limit ($k_c h \ll 1$, see figure 15), there is no mode selection. The centrifugal instability amplifies indifferently a broad plateau of length scales λ, provided they are larger than a given cut-off scale, which we can determine: the minimal critical wavelength λ_c (which is thus estimated from

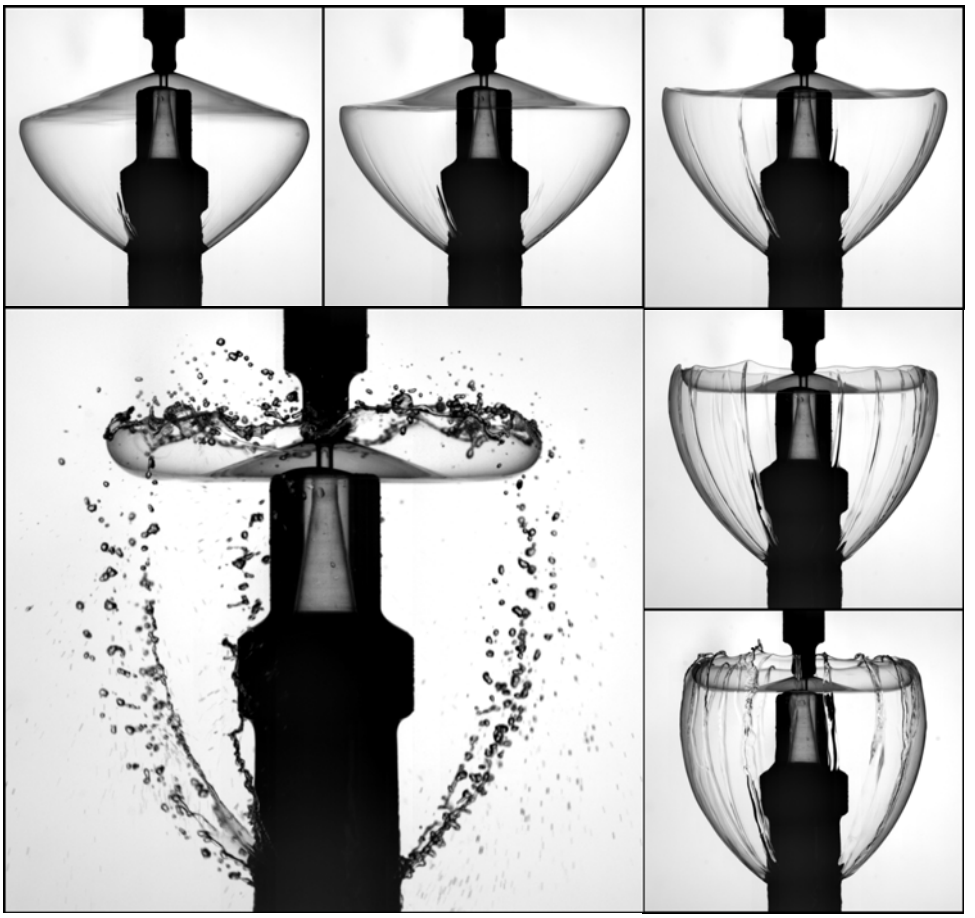

FIGURE 16. Sequence: non-stationary water bell transiting by a jagged shape over which particularly marked wrinkles develop. These azimuthal deformations then provoke the puncture of the sheet, and its destruction, as seen on the last image of the sequence (see also '*Fig. 14*' in figure 1). Images are separated by a time interval of 21.5 ms and their width corresponds to 110 mm. Enlargement: The wrinkles are evidenced immediately after the bell fragmentation by the spatial organization of the drops.

the maximal local curvature $|\kappa_\theta|$ of the bell profile), i.e.

$$\lambda > \lambda_c = 2\pi\sqrt{\frac{\sigma}{\rho|\kappa_\theta|u^2}} \approx 1\,\text{mm}. \tag{5.16}$$

All of this is consistent with the observed multiscale drapes downstream from the cusp (all spaced by a distance larger than λ_c) which can be as large as 10 to 20 times λ_c, and with the fact that their amplification happens on a portion of the bell profile whose curvature varies continuously from zero at the first inflection point to the maximal value we used above.

We note finally that this instability could possibly be associated with the energy dissipation mechanism in the jump (equation (4.9)).

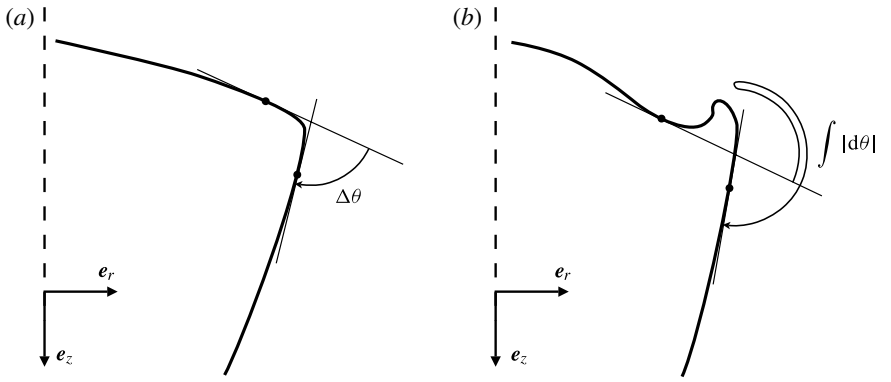

FIGURE 17. Illustration of the 'absolute' curvature sum $\int |\mathrm{d}\theta|$ seen by a liquid particle in motion along the fold profile. (*a*) For an integrally convex bell. (*b*) For a crumpled bell.

6. Conclusions and extension

The observation of stationary axi-symmetrical pressurized bells formed by the impact of a liquid jet on a solid disc and exhibiting uncommon sharp and pointed shapes was the starting point of this study. We found that the surprising and easily observable trajectory of the fluid particles presenting two successive inflection points can only be understood by renouncing the usual assumption that the sheet thickness h is infinitely small in comparison with the sheet characteristic radius of curvature κ_θ^{-1}.

This led us to consider the influence of the flow velocity profile in a sheet cross-section. For a local Weber number $We = \rho h u^2/\sigma$ larger than 2 and a plug flow profile (as expected in the present case where viscous damping and relative curvature variation rates seen by a fluid particle in motion are of the same order) three distinct local curvatures permit to equilibrate a given bell excess internal pressure for a given flow rate carried by the sheet.

The transition from a 'small' curvature solution to a 'large' curvature solution of opposite sign is found to be compatible with global balances of mass, linear and angular momenta. For an upstream local Weber number We_1 larger but close to 2 as one naturally finds at the maximal extension of a crumpled bell, we furthermore showed that the measured pressure and curvatures are quantitatively in agreement with the predictions of our description.

In addition, the viscous dissipation occurring at this sudden curvature inversion triggers a flow transition from a super ($We_1 > 2$) to a subcritical regime ($We_2 < 2$) with respect to sinuous capillary waves in agreement with the receding velocities $u_1 > V_1$ and $u_2 < V_2$ observed in each region, respectively. This confers to the transition the original status of a capillary hydraulic jump on a freely suspended liquid sheet.

The azimuthal wrinkles corresponding to thickness modulations of the sheet that develop at the jump are identified with the varicose mode of an inertial, Rayleigh–Taylor destabilization of the sheet. They form in response to the centripetal acceleration the strong curvature at the jump imposes to the liquid as it flows along the bell profile.

As a concluding remark, we would like to relate the situation of closed crumpled bells with that of an 'open liquid bell' (i.e. a Savart sheet) developing at large injection Weber number in a non-evanescent medium at rest ($We_0 \gtrsim 1000$ for a water sheet in air), which is the working regime of most industrial atomization processes (Lefebvre 1989), and naturally formed liquid sheets. It is well known that in this condition the

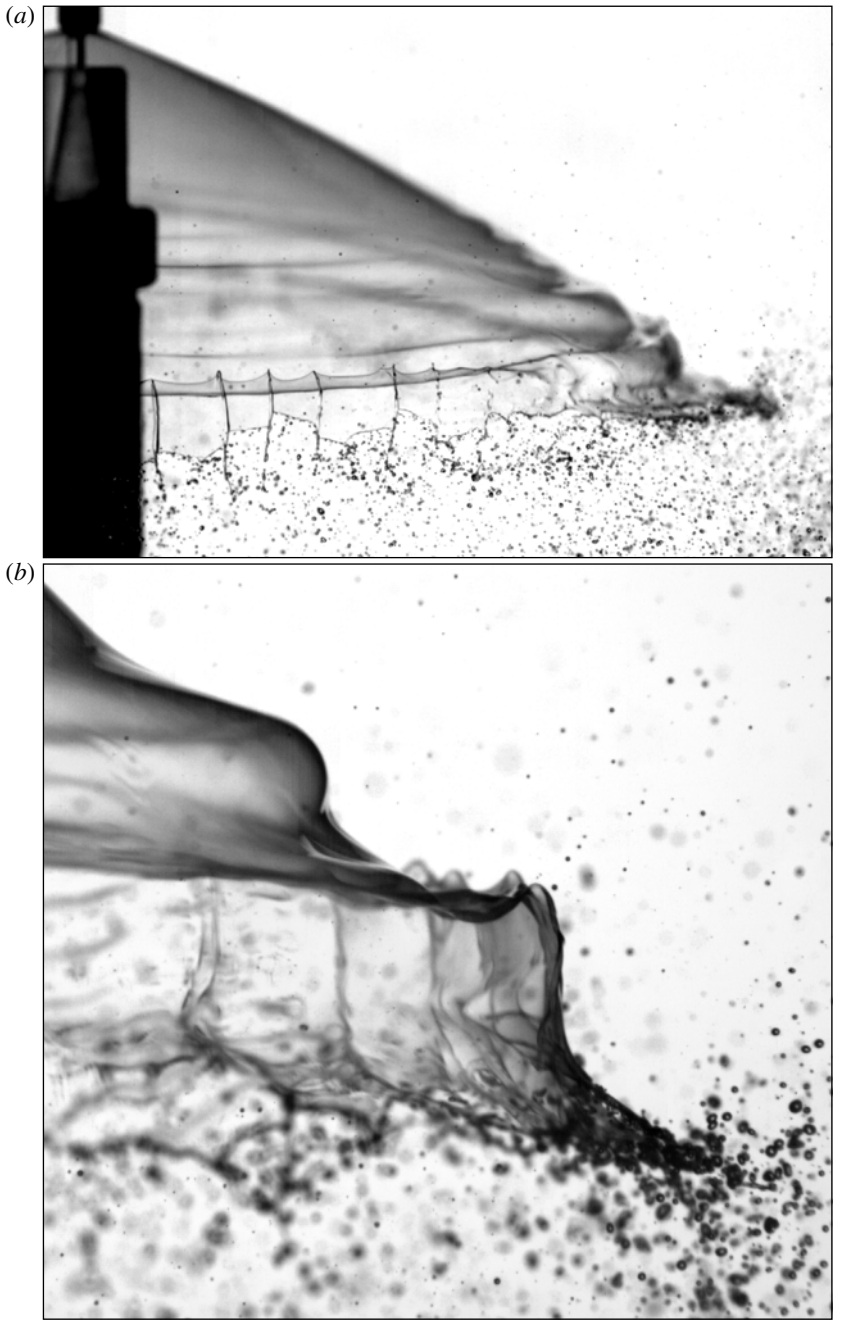

FIGURE 18. (*a*) A conical water Savart sheet (which can be seen as an 'open bell') at large injection Weber number We_0 naturally flapping due to its shear interaction with the ambient air at rest. (*b*) Lateral view of the grown flapping waves at the periphery emphasizing the large curvature at the crest and the azimuthal wrinkles it induces.

rapidly flowing liquid sheet develops flag-like flapping waves excited by the shear with the ambient medium; a destabilization known as Squire destabilization in the context

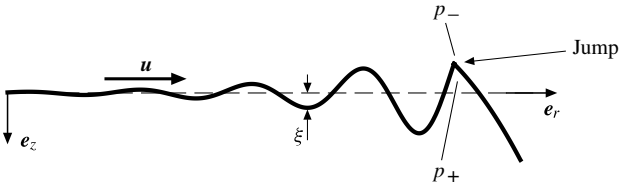

FIGURE 19. Sketch of a planar liquid sheet flapping as it flows in air at rest. The air flow associated with the flapping wave propagation sets a pressure difference between both sides of the sheet: relative to the static ambient pressure, crests are in suction (here at the jump $p_- < 0$ since $\xi < 0$) while troughs are under excess pressure ($p_+ > 0$ still for $\xi < 0$) according to equation (6.1). At the kink visible on the last wave crest (see also figure 18) the excess pressure is thus on the side opposite to that of the curvature centre exactly as for crumpled bells, and this kink can therefore be interpreted as an hydraulic jump similar to that occurring on a crumpled bell.

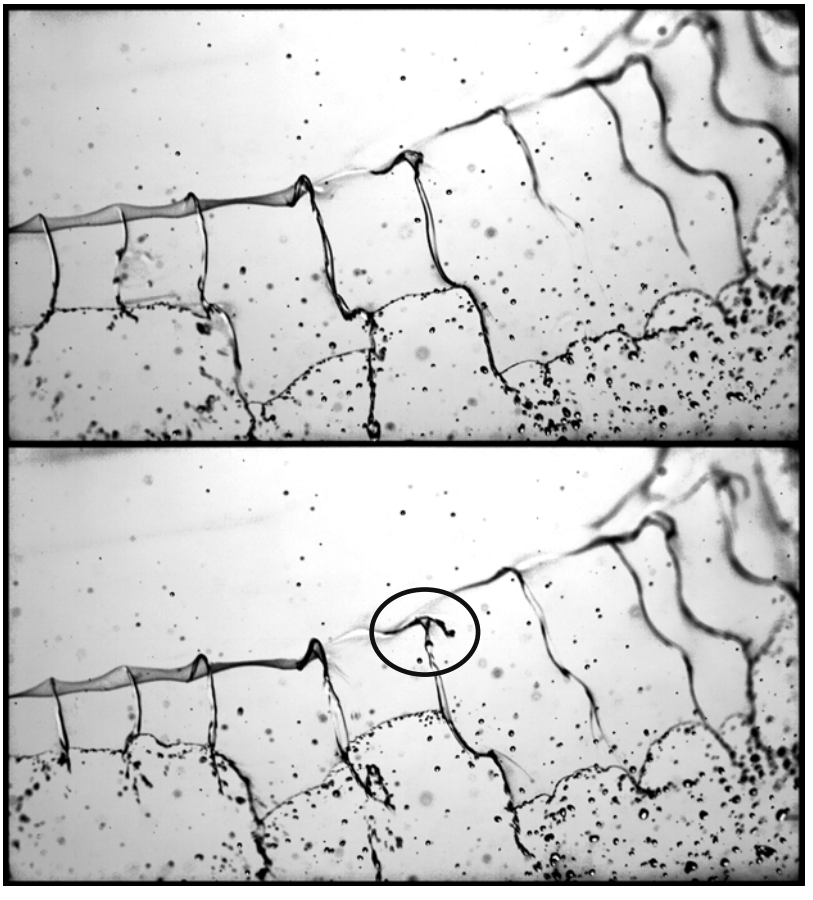

FIGURE 20. Focus on the periphery of a flapping Savart liquid sheet identical to that of figure 18. The azimuthal thickness modulations or wrinkles develop at the crest of the flapping wave in response to the transverse acceleration imparted to the fluid particles at the passage of the crest. Note the striking resemblance of the pattern with that of figure 16 and the circled ligament centrifugation event similar to that of figure 13.

of thin liquid sheets (Squire 1953; Huang 1970; Villermaux & Clanet 2002; Lhuissier & Villermaux 2009). As figure 18 illustrates, the flapping wave amplitude increases strongly with the distance from the jet until the wave crest shapes into a sharp bend.

At this sharp bend, in the very same way as for crumpled bells, the transverse acceleration of the flowing liquid is so large that azimuthal thickness modulations (visible as wrinkles in figure 20) form. This is the 'wavy corridor' mechanism (Bremond, Clanet & Villermaux 2007; Lhuissier & Villermaux 2009). We argue that the sharp bend clearly visible on the bottom picture of figure 18 can be understood as a hydraulic jump since the local conditions on the sheet are qualitatively the same as those triggering the jump on crumpled bells.

Indeed as for a usual Kelvin–Helmholtz destabilization, the growth of a flapping (or sinuous) mode on the sheet is associated with a pressure difference between its two sides, actually the consequence of the destabilization mechanism itself: as a wave propagates the pressure in the surrounding air, which is set into motion by the moving pattern, is modulated by a classical Bernoulli effect. Noting ξ the local sheet position in the perpendicular direction $\boldsymbol{e}_z$ and p_+ and p_- the air pressure at the interface on the sides $z > 0$ and $z < 0$ respectively (see figure 19), the linear development of the flapping instability on an infinite sheet flowing at a velocity u in the at rest air of density ρ_a yields

$$p_+ = -p_- = -\rho_a u^2 \frac{\xi}{\ell} \quad \text{with } \ell = \frac{\sigma}{\rho_a u^2} \tag{6.1}$$

valid for a sinuous mode in the limit $\rho_a/\rho \ll 1$, $h/\ell \ll 1$ and $\rho h u^2/\sigma \gg 2$. Equation (6.1) simply expresses that the air pressure is locally smaller on the side of the crest than on the side of the trough. The situation on a flapping sheet is therefore like that of crumpled bells: just before a crest the excess pressure is on the side opposite to that of the curvature centre and, for the reasons we have explained, a curvature inversion is likely to occur. This is the origin of the sharp bend in figure 18 connecting two portions of opposite curvatures.

The crumpled bell, which is an exception in the broad set of shapes discovered by Félix Savart, thus appears as a laboratory to understand the singular phenomena at the edge of free flapping sheets, for which they are the rule.

REFERENCES

Bohr, T., Dimon, P. & Putkaradze, V. 1993 Shallow-water approach to the circular hydraulic jump. *J. Fluid Mech.* **254**, 635–648.

Bond, W. N. 1935 The surface tension of a moving water sheet. *Proc. Phys. Soc.* **47**, 549–558.

Bond, W. N. & Puls, H. O. 1937 The change of surface tension with time. *Phil. Mag.* **24**, 864–888.

Boussinesq, J. 1869*a* Théories des expériences de Savart, sur la forme que prend une veine liquide après s'être choquée contre un plan circulaire I. *C. R. Acad. Sci. Paris* **69**, 45–48.

Boussinesq, J. 1869*b* Théories des expériences de Savart, sur la forme que prend une veine liquide après s'être choquée contre un plan circulaire II. *C. R. Acad. Sci. Paris* **69**, 128–131.

Bremond, N., Clanet, C. & Villermaux, E. 2007 Atomization of undulating liquid sheets. *J. Fluid Mech.* **585**, 421–456.

Bremond, N. & Villermaux, E. 2005 Bursting thin liquid films. *J. Fluid Mech.* **524**, 121–130.

Brunet, P., Clanet, C. & Limat, L. 2004 Transonic liquid bells. *Phys. Fluids* **16** (7), 2668–2678.

Buckingham, R. & Bush, J. W. 2001 Fluid polygons. *Phys. Fluids* **13**, S10.

Bush, J. W. & Aristoff, J. 2003 The influence of surface tension on the circular hydraulic jump. *J. Fluid Mech.* **489**, 229–238.

BUSH, J. W., ARISTOFF, J. & HOSOI, A. 2006 An experimental investigation of the stability of the circular hydraulic jump. *J. Fluid Mech.* **558**, 33–52.

CLANET, C. 2001 Dynamics and stability of water bells. *J. Fluid Mech.* **430**, 111–147.

CLANET, C. 2007 Waterbells and liquid sheets. *Annu. Rev. Fluid Mech.* **39**, 469–496.

DARRIGOL, O. 2005 *Worlds of Flow: A History of Hydrodynamics from the Bernoullis to Prandtl*. Oxford University Press.

ELLEGAARD, C., HANSEN, A. E., HAANING, A., HANSEN, K., MARCUSSEN, A., BOHR, T., HANNSEN, J. L. & WATANABE, S. 1998 Creating corners in kitchen sinks. *Nature* **392**, 767–768.

HOPWOOD, F. L. 1952 Water bells. *Proc. Phys. Soc.* B **65**, 2–5.

HUANG, J. C. P. 1970 The break-up of axisymmetric liquid sheets. *J. Fluid Mech.* **43**, 305–319.

KELLER, J. B. & KOLODNER, I. 1954 Instability of liquid surfaces and the formation of drops. *J. Appl. Phys.* **25** (7), 918–921.

LANCE, G. N. & PERRY, R. L. 1953 Water bells. *Proc. Phys. Soc.* B **66**, 1067–1072.

LAPLACE, P. S. 1805 *Sur l'action capillaire, supplément au livre X du Traité Mécanique Céleste, t. IV*. Courcier.

LEFEBVRE, A. H. 1989 *Atomization and Sprays*. Hemisphere.

LHUISSIER, H. & VILLERMAUX, E. 2009 Soap films burst like flapping flags. *Phys. Rev. Lett.* **103**, 054501–(4).

LORD RAYLEIGH, J. W. 1914 On the theory of long waves and bore. *Proc. R. Soc. Lond.* A **90**, 324–328.

NEWTON, I. 1687 *Philosophiae Naturalis Principia Mathematica*. London.

PARLANGES, J.-Y. 1967 A theory of water-bells. *J. Fluid Mech.* **29**, 361–372.

PULS, H. O. 1936 The surface tension of a moving mercury sheet. *Phil. Mag.* **22**.

ROWLINSON, J. S. 2002 *Cohesion*. Cambridge University Press.

SAVART, F. 1833*a* Mémoire sur le choc d'une veine liquide lancée contre un plan circulaire. *Ann. Chim.* **54**, 56–87.

SAVART, F. 1833*b* Suite du mémoire sur le choc d'une veine liquide lancée contre un plan circulaire. *Ann. Chim.* **54**, 113–145.

SQUIRE, H. B. 1953 Investigation of the stability of a moving liquid film. *Br. J. Appl. Phys.* **4**, 167–169.

TAYLOR, G. I. 1959*a* The dynamics of thin sheets of fluid I. Water bells. *Proc. R. Soc. Lond.* A **253**, 289–295.

TAYLOR, G. I. 1959*b* The dynamics of thin sheets of fluid III. Desintegration of fluid sheets. *Proc. R. Soc. Lond.* A **253**, 313–321.

VILLERMAUX, E. & CLANET, C. 2002 Life of a flapping liquid sheet. *J. Fluid Mech.* **462**, 342–363.

WATSON, E. J. 1964 The radial spread of a liquid jet over a horizontal plane. *J. Fluid Mech.* **20**, 481–499.